Trace element enrichment mechanisms in black shales during the early Cambrian (ca. 521–514 Ma), South China

Wang, Zhanghu; Tan, Jingqiang; Hilton, Jason; Dick, jeffrey; Wen, Zhigang

DOI:
10.1016/j.marpetgeo.2022.106083

Document Version
Peer reviewed version

Citation for published version (Harvard):
Wang, Z, Tan, J, Hilton, J, Dick, J & Wen, Z 2023, 'Trace element enrichment mechanisms in black shales during the early Cambrian (ca. 521–514 Ma), South China', *Marine and Petroleum Geology*, vol. 149, 106083. https://doi.org/10.1016/j.marpetgeo.2022.106083

Trace element enrichment mechanisms in black shales during the early Cambrian (ca. 521–514 Ma), South China

Zhanghu Wang[1,2], Jingqiang Tan[2,*], Jason Hilton[3], Jeffrey Dick[2], Zhigang Wen[1],

[1] Cooperative Innovation Center of Unconventional Oil and Gas, Yangtze University, Wuhan, 430100, China

[2] School of Geosciences and Info-Physics, Central South University, Changsha 410083, China

[3]School of Geography, Earth and Environmental Science, University of Birmingham, Birmingham, B15 2TT, UK

* Corresponding author: Jingqiang Tan

E-mail address: tanjingqiang@csu.edu.cn

ABSTRACT

It is widely accepted that significant perturbations in ocean redox states are closely related to biological evolution during the early Cambrian. However, the host and geochemical cycle of redox-sensitive elements (V and Zn) of the Niutitang Formation shale in South China have not been well-constrained. This study reports lithofacies, mineralogy and geochemical data of high-resolution samples from slope and basin settings (Xa1 and Xb1 wells, Hunan Province), to evaluate the significance of redox condition and hydrothermal contribution to trace element accumulation during the early Cambrian. Our results reveal the Zn-rich host is primarily sphalerite, while the V-rich host includes organic matter, illite, and anatase minerals in the Niutitang shale. Illite and anatase minerals have significant V concentration (14.8% and 18.3%), whereas organic matter contains relatively lower V concentration (1.4%). Trace elements can be scavenged by dissolved organic matter in seawater, and then taken up by clay minerals or form sulfide during deposition/diagenesis of organic-rich shales. Although seawater restriction of the lower member (LM) shale was stronger than in the upper member (UM) shale, euxinic conditions were more conducive to V and Zn enrichment than ferruginous conditions. Specifically, dwindling concentrations of V and Zn in seawater existed in South China during deposition of the early LM shale. However, the ocean experienced episodic hydrothermal activity, which may have supplied abundant trace elements to supplement seawater content. Overall, we propose that the V and Zn geochemical cycles in the early Cambrian paleo-ocean were controlled by redox condition, organic matter, and the trace element inventory of seawater.

Keywords: Niutitang shale, free H_2S content, hydrothermal input, seawater restriction, trace element inventory

1. Introduction

Redox-sensitive trace elements (TEs: Mo, U, V, Zn) in sediments can be used to infer oxygen concentration in the overlying water column or atmosphere, and have been widely used as proxies for redox conditions in ancient oceans (Jones and Manning, 1994; Algeo and Maynard, 2004; Tribovillard et al., 2006; Scott et al., 2017; Algeo and Liu, 2020). TEs are commonly reduced from high to low valence state under low-oxygen conditions, and may be complexed with organic acids, adsorbed by authigenic sulfides, or precipitated in the form of insoluble oxyhydroxides (Tribovillard et al. 2006; Algeo and Liu, 2020). The geochemical cycle of TEs in the paleo-ocean system is complex and influenced by various factors including terrigenous supply, oceanic metal inventory, seawater restriction, redox condition, and volcanic/hydrothermal input (You et al., 1996; Algeo and Tribovillard, 2009; Gill et al., 2011; Cheng et al., 2016; Zou et al., 2018; Paschall et al., 2019). Ferruginous water masses (anoxic condition without free H_2S) are comparatively common in early Cambrian or older geological time intervals (Canfield, 1998; Algeo and Li, 2020), while euxinic environments have appeared several times in geological history and modern ocean systems (Feng et al., 2014; Li et al., 2019). Anoxic oceans in different periods of geological history may exhibit unique trace element enrichment and migration patterns.

The early Cambrian is one of the most critical periods of biological radiation in Earth history. During the Cambrian Stage 3, from ~521–514 Ma, a marine transgression event resulted in the widespread deposition of black shale across South China. This black shale is exceptionally rich in organic carbon and contains unusual concentrations of V and Zn (Guo et al., 2016; Fan et al., 2020). Previous research has shown that a "euxinic wedge" developed in the early Cambrian paleo-ocean (Li et al., 2010, 2015, 2020; Feng et al., 2014) in which the surface, middle, and deep layers of the ocean were characterized by oxic, euxinic, and ferruginous conditions, respectively (Jin et al., 2016). Han et al (2018) analyzed the geochemical cycle of the element vanadium (V) in the Longbizui and Duoding sections and suggested that the drawdown of trace elements in seawater may have affected V enrichment in the black shale. However, the

host and enrichment pattern of vanadium in ferruginous and euxinic environments has not been evaluated during the early Cambrian. In addition, the seawater was also strongly affected by multiple episodes of volcanic and hydrothermal activity during the early Cambrian (Chen et al., 2009; Liu et al., 2015; Gao et al., 2018; Wang et al., 2020a; Tan et al., 2021; Xie et al., 2021). Submarine hydrothermal processes in the early Cambrian have been suggested to explain bedded polymetallic Ni–Mo–PGE mineralization (Coveney and Chen, 1991; Li and Gao, 2000; Jiang et al., 2006), extreme element accumulation in sedimentary rocks (Guo et al., 2016; Han et al., 2017), and biological evolution (Wang et al., 2020b). Hydrothermal activity with hot, volatile-rich components may have changed the chemical conditions of the seawater and affected trace element enrichment and migration. However, the influence of hydrothermal activity, redox condition, and seawater restriction on the geochemical cycle of trace elements is still poorly understood.

The lower Cambrian black shales in South China offer favorable conditions for analyzing the geochemical cycle of trace elements in an anoxic stratified paleo-ocean. The bulk-rock geochemical data are conducive to reconstructing unique environmental constraints during the early Cambrian. Here, the main purpose of this study is to analyze the host of V and Zn elements using micro-analytical techniques at a micro- and nano-scale from two wells in South China, then provide new insights into significance of redox condition, seawater, and hydrothermal contribution to trace elements accumulation in organic-rich shales.

2. Geological setting

During the Ediacaran–Cambrian transition period, the South China Craton was composed of the Yangtze and Cathaysia blocks. From modern northwest to southeast, the depositional environments in the Nanhua Basin ranged from shallow- to deep-water areas comprising mainly carbonate platform, shelf, slope and basin settings (Goldberg et al., 2007; Li et al., 2008; Okada et al., 2014). Lithologies in the shallow-water areas were dominated by gray dolomite and limestone, while the deep-water areas were

dominated by gray-black shale and chert (Figure 1A). During the early Cambrian Stage 3, a global transgression event submerged the previously deposited carbonate platform, resulting in the development of organic-rich shale facies across South China (Figure 1B). These organic-rich shales comprise the laterally equivalent Niutitang, Yu'anshan, and Xiaoyanxi formations (Figures 1, 2). Deposition of the shale facies was accompanied by hydrothermal activity (Liu et al., 2015), which may have caused the intermittent development of a Ni-Mo metal layer in South China. The Ni-Mo metal layer has been used as an important marker for stratigraphic correlation (Xu et al., 2011; Han et al., 2020). With the gradual decline of sea level after 518 Ma, the lithology of the upper Niutitang, Yu'anshan, and Xiaoyanxi formations was dominated by grey siltstone and shale (Figure 2).

The shale interval selected in this paper developed after the early Cambrian transgression event (521–514 Ma) and is located above the Ni-Mo layer. According to high-resolution petrology, biostratigraphy, isotope dating, and inorganic geochemistry of nine sections across South China, our previous studies have determined the development period of the lower member (LM) of the Niutitang, Yu'anshan, and Xiaoyanxi formations was from 521–518 Ma, and the upper member of (UM) was from 518–514 Ma (Figure 2, Jiang et al., 2012; Yang et al., 2018; Wang et al., 2020a). The Xa1 and Xb1 wells in our study area, and another seven sections distributed across the inner shelf to basin depositional facies, have been selected to analyze the geochemical cycling of V and Zn elements in the paleo-ocean (Figure 1C). These comprise the Meishucun (Jenkins et al., 2002; Yang et al., 2003; Wen et al., 2015) and Xiaotan sections in Yunnan Province (Och et al., 2013), the Xy1 well (Li et al., 2018) and the Jinsha section in Guizhou Province (Jin et al., 2016), and the Yangjiaping (Cheng et al., 2016), Longbizui (Wang et al., 2012) and Yuanjia sections in Hunan Province (Cheng et al., 2020).

3. Materials and methods

The Xa1 well in Anhua County (111°26′12″E, 28°17′58″N) and the Xb1 well in

Jishou County (109°49′15″E, 28°23′03″N), South China, were located in different depositional facies during the early Cambrian. We have selected 50 samples from the two wells for geochemical analyses. All samples were crushed into powder for analyses of total organic carbon (TOC), total sulfur (TS), major elements, and trace elements.

Concentrations of major oxides (SiO_2, Al_2O_3, Fe_2O_3, P_2O_5, and MnO) were determined by X-ray fluorescence (XRF) on molten glass beads at Central South University. For major oxides with concentrations greater than 0.3%, the accuracy was better than 2%. Trace elements (Mo, U, V, and Zn) were determined by ICP-MS at Societe Generale de Surveillance S.A. (SGS). A 50 mg sample powder was dissolved in a high-pressure Teflon bomb with 1 ml HF and 2 ml HNO_3 at 190 °C for 48 h. After removing HF by heating, the residue was dissolved in 2 ml H_2O and 2 ml HNO_3 at 145 °C for 12 h. Analytical precision was better than 10 % relative standard deviation.

For measurements of TOC and TS content, 100 mg samples were first treated with excess hydrochloric acid solution (volume ratio 1:7), and then washed with distilled water to remove the HCl. TOC content was determined using a high-frequency infrared carbon and sulfur analyzer (LECO CS-744) at Central South University. For TS measurements, separate 100 mg samples, not treated with HCl, were dried more than 2 h at 105 °C. Then, TS content was measured on a carbon and sulfur analyzer. The analytical precision was better than 0.2 %.

For sulfide mineral identification, the selected samples were firstly cut into 1 cm^3 cubes with a cutting machine. Then the surface to be observed was ground, polished, and sprayed with a carbon coating. Finally, a FEI Quanta 200 Scanning Electron Microscope (SEM) with Energy Dispersive Spectrometer (EDS) at China University of Geosciences, Wuhan was used to identify the minerals in shale and perform elemental mapping. The element content of every metallic mineral was tested to determine its host.

Enrichment factors (EF) were calculated based on the ratio between trace element concentration and aluminum (Al) within the sample, compared to the same ratio in Upper Continental Crust (UCC) (Tribovillard et al., 2006; Algeo and Tribovillard, 2009). The equation is as follows:

$$X_{EF} = [(X/Al)_{sample}) /(X /Al)_{ucc}]$$

where UUC data for normalization were taken from McLennan (2001), and X_{EF}> 1.0 and X_{EF}< 1.0 indicate enrichment and depletion of X element, respectively.

4. Results

4.1. Metallic minerals in black shale

In order to analyze the types of metallic minerals present in the lower Cambrian black shale, minerals from samples in the Xa1 and Xb1 wells have been preliminarily identified. The main sulfur-bearing mineral is pyrite that forms clumps and bands (Figure 3). The Ba-bearing minerals in the study area are mainly celsian and hyalophane (Figures 3B, C, I). There are also some sulfur-bearing minerals, such as barite (Figures 3D, E). The barite minerals are rare and do not exhibit obvious metasomatic residual structure. The element Zn exists mainly in the form of sphalerite, and can be seen in low concentration in several samples (Figure 3H).

In addition, we found that the element V is mainly enriched in organic matter (Figure 4A), illite (Figure 4B) and the mineral anatase (Figures 4C, 4E, 4F) from black shales the study area. The element V can also be scavenged by dissolved organic matter in seawater, and then taken up by clay minerals during transport or deposition (Lu et al., 2021). Furthermore, V can replace the element Ti in anatase with isomorphism. The V content in the anatase mineral is relatively higher (18.3%), while that in organic matter is relatively lower (1.4%, Figure 4D).

4.2. TOC and TS contents

The TOC and TS contents of the Niutitang shale from the Xa1 and Xb1 wells are shown in Figures 5 and 6 and the Supplementary Data. From the Xa1 well, LM shale TOC contents range from 8.1–31.5 % (avg. 14.0 %) and TS contents range from 0.4–2.6 % (avg. 0.9 %), while in the UM shale TOC contents range from 2.6–8.1 % (avg. 5.1 %) and TS contents range from 1.5–3.8 % (avg. 2.3 %). From the Xb1 well, LM shale TOC contents range from 1.4–12.4 % (avg. 5.5 %) and TS content range from

1.2– 5.3 % (avg. 2.6 %), whereas in the UM shale TOC contents range from 0.8–2.1 % (avg. 1.6 %) and TS contents range from 1.3–1.7 % (avg. 1.4 %).

4.3. Trace elements

Trace element concentrations and Mo_{EF}/U_{EF} values can be seen in Figures 5 and 6. The Niutitang shale exhibits variable Mo, U, V, Zn concentrations in the Xa1 and Xb1 wells. In the LM shale from the Xa1 well, concentrations range from 29–506 ppm for Mo, 30–209 ppm for U, 308–4075 ppm for V, and 21–3145 ppm for Zn. Enrichment factors of theses trace elements are 90–678 for Mo_{EF}, 28–586 for U_{EF}, 7–145 for V_{EF}, and 1–231 for Zn_{EF}. The Mo_{EF}/U_{EF} ratio in the LM shale is 0.4–6.7 (avg. 2.3). In contrast, the UM shale in the Xa1 well exhibits relatively lower Mo (24–76 ppm), U (8–46 ppm), V (103–348 ppm), and Zn (16–64) concentrations. The Mo_{EF}/U_{EF} ratio in the UM shale is 3.1–6.0 (avg. 5.3) and is higher than in the LM shale. Similar features of the trace element concentrations and Mo_{EF}/U_{EF} ratios are exhibited in the Xb1 well. From the Xb1 well, Mo content is > 100 ppm at the bottom of the LM shale, and < 25 ppm in the UM shale. Additionally, the V_{EF} and Zn_{EF} is 1.6–18.3 (avg. 6.0) and 1.4–13.4 (avg. 3.5) in the LM shale, and 1.2–2.5 (avg. 1.5) and 1.4–2.0 (avg. 1.7) in the UM shale, respectively. Like the Xa1 well, in the Xb1 well the Mo_{EF}/U_{EF} ratio is lowest in the LM shale (1.0–9.3, avg. 4.1), and higher in the UM shale (3.0–6.5, avg. 4.8).

5. Discussion

5.1. Redox conditions during the early Cambrian

Analysis of redox state is an important paleoenvironmental method, which mainly includes iron speciation (Raiswell et al., 1988; Poulton and Canfield, 2005), redox-sensitive trace element geochemistry (Scott and Lyons, 2012), and assessment of Mo–U enrichment factor (Mo_{EF} and U_{EF}) data (Tribovillard et al., 2006, 2012; Algeo and Tribovillard, 2009). Scott and Lyons (2012) systematically evaluated Mo geochemistry in modern anoxic basin systems and suggested that Mo content < 25 ppm indicates an oxic condition; 25–100 ppm indicates intermittent or seasonal euxinic conditions; while

Mo content >100 ppm indicates a persistent euxinic condition. The enrichment factors of Mo and U are generally lower than 10 in suboxic conditions, and higher in anoxic conditions. Here, the Mo_{EF} -U_{EF} correlation was mainly used to constrain the redox condition for the LM and UM shales of the Niutitang Formation in the study area (Figure 7).

5.1.1. Redox condition of the LM shale

The Mo_{EF}-U_{EF} correlation of the LM shale in the Xa1 and Xb1 wells can be seen in Figure 7. Almost all samples in the Xa1 well are characterized by high Mo content (>100 ppm), U content (30–207 ppm), Mo_{EF} (90–678) and U_{EF} (30–207). The Mo_{EF}/U_{EF} ratio is between 1 and 3 times that of modern seawater (Figure 7A). These characteristics suggest a euxinic environment persisted during the depositional period of the LM shale in the Xa1 well. The Yuanjia section is close to the Xa1 well (Cheng et al., 2020), and its iron speciation data are Fe_{HR}/Fe_T =0.88-1 (avg. 0.98) and Fe_{Py}/Fe_{HR}=0.58–0.97 (avg. 0.89). The trace elements data in the Xa1 well are consistent with the iron speciation data in the Yuanjia section, both indicating extremely euxinic conditions in the basin facies from 521–518 Ma (Figure 8). The Mo_{EF}/U_{EF} ratio of the LM shale in the Xb1 well is between 0.1 and 0.3 times that of modern seawater (Figure 7B). Due to the TOC, Mo, U, and V contents, and Mo_{EF}-U_{EF} variation, the LM shale of the Niutitang Formation in the Xb1 well can be divided into the LM-1 and LM-2 submembers (Figure 6). The LM-1 submember shale in the Xb1 well exhibit high Mo content (>100 ppm), Mo_{EF} (65–142), and U_{EF} (21–100), which suggest a euxinic environment. The Longbizui section is adjacent to the Xb1 well (Figure 1), and its iron speciation data also show Fe_{HR}/Fe_T =0.79-1.13 (avg. 0.98) and Fe_{Py}/Fe_{HR}=0.13–0.86 (avg. 0.51), indicating a ferruginous to euxinic condition (Wang et al., 2012). In addition, the LM-2 submember shale in the Xb1 well are characterized by moderate Mo (2–41 ppm), U (3–11 ppm), Mo_{EF} (2–37), and U_{EF} (2–8) contents, which are consistent with the iron speciation data (Fe_{HR}/Fe_T =0.21–1.4 (avg. 0.82) and Fe_{Py}/Fe_{HR}=0.01–0.69 (avg. 0.33) in the Longbizui section (Figure 7B). Both of these lines of evidence above suggest a ferruginous with intermittent euxinic condition existed in the slope facies

204 from 521–518 Ma.

205

206 5.1.2. Redox condition of the UM shale

207 In the Xa1 well, the UM shale is characterized by Mo content between 24 and 76
208 ppm and is consistently higher than 25 ppm. The Mo_{EF} and U_{EF} are also relatively high
209 and can reach up to 86 and 28, respectively, indicating a ferruginous condition (Figure
210 7A). The Mo_{EF}/U_{EF} ratio is between 1 and 3 times that of modern seawater. Due to the
211 gradual decline of sea level, the redox proxies shows that the water column in the basin
212 facies changed from a euxinic to ferruginous condition from 518–514 Ma. In addition,
213 the Mo content of the UM shale in the Xb1 well is generally lower than 25 ppm. The
214 Xb1 well also exhibits relatively low Mo_{EF} (7–16) and U_{EF} (2–4), suggesting a suboxic
215 environment persisted during the depositional period of the UM shale.

216

217 5.1.3. Evolution of redox conditions in the Nanhua Basin from 521–514 Ma

218 The redox conditions of the other seven sections considered here have been
219 systematically analyzed with iron speciation and redox-sensitive trace element data
220 (Jenkins et al., 2002; Yang et al., 2003; Och et al., 2013; Wen et al., 2015; Jin et al.,
221 2016; Li et al., 2018; Cheng et al., 2020). As shown in the redox proxy comparison
222 from the inner shelf to basin setting in Figure 8, the depositional environment was
223 characterized by euxinic conditions during the LM shale deposition period. In addition,
224 an oxic environment first appeared in the inner shelf facies (i.e., Meishucun and Xiaotan
225 sections) during the late LM shale depositional period, pre-dating the "Cambrian
226 explosion" (Jin et al., 2016; Xiang et al., 2017). It is plausible that it took time for life
227 to adapt to the newly increased oxygenation levels with a delay until lifeforms reached
228 a critical threshold before undergoing an explosive evolutionary radiation. Depositional
229 environments of the outer shelf facies were characterized by intermittent euxinic
230 conditions, while basin facies were characterized by persistent euxinic conditions.
231 During the UM shale deposition period, oxic conditions gradually spread from inner
232 shelf to outer shelf facies (i.e., Jinsha section and Xy1 well, Figure 8). Additionally,

there was no free sulfur in the water column, and euxinic environments were not obvious during this time interval. The water column exhibited ferruginous conditions in the basin setting (i.e., Yuanjia section and Xa1 well). Subsequently, marine environments were dominated by oxic conditions in South China, which were conducive to biological reproduction during the deposition of the late UM shale.

5.2. Seawater restriction

Mo generally has an average concentration of 1.5 ppm and presents as stable state with a high valence (VI, MoO_4^{2-}) in oxic conditions (Taylor and McLennan, 1995). In an anoxic water column, Mo is reduced to MoO_2^{+} or $MoO_xS_{4-x}^{2-}$, and the latter may be formed as organic thiomolybdate, or further reduced to MoS_4^{2-} (Brumsack, 1989; Adelson et al., 2001; Algeo and Rowe, 2012). Mo has a long residence time in water (approximately 731 kyr). This unique feature of Mo is commonly used to assess the restriction of modern and ancient seawater (Tribovillard et al., 2012; Zhao et al., 2016). The relationship between Mo and TOC can reveal the degree of anoxic water restriction (Figure 9).

During the depositional period of the LM shale, the Mo/TOC ratio of the Xb1 well (1–24, avg. 11.5) is higher than the present-day value of the Framvaren Basin (Mo/TOC = 9), indicating a moderately restricted water environment (Figure 9B). However, there is no obvious correlation between the Mo content and TOC content in the LM shale of the Xa1 well. The Mo-TOC covariant relationships of the Xa1 well cannot be used to assess watermass restriction. The Yuanjia section is close to the Xa1 well, and its Mo/TOC ratio is close to Black Sea Basin (Mo/TOC=4.5), indicating a moderately to strongly restricted water environment (Chen et al., 2022). However, Cheng et al. (2020) found that the authigenic Mo and U content in the black shale of the Yuanjia section were not depleted, and the normal-marine-like Mo/U ratios (1× SW) are also similar to the Xa1 well (Figure 7A). It is noteworthy that the Mo_{EF}-U_{EF} correlation of the modern Cariaco Basin or Saanich Inlet Basin are not significant. The paleo-ocean in South China also suffered from multiple phases of hydrothermal activity (see Section

5.4), which may have provided abundant trace elements during the early Cambrian (Han et al., 2017). The Mo_{EF}-U_{EF} correlation of basin facies shows these may have been affected by hydrothermal activity, and the seawater should be moderately to strongly restricted during the depositional period of LM shale. Figure 9A shows a modest correlation that is interpretable in terms of watermass restriction degree of the UM shale. The Mo/TOC ratio of the Xa1 shale was 5–9 (avg. 8), and indicated a moderate seawater restriction, closer to the Framvaren Fjord Basin conditions during the depositional period of the UM shale. The depositional environment was also weakly restricted in the Xb1 well (Figure 9A).

5.3. Geochemical cycling of trace elements in the paleo-ocean from 521–514 Ma

5.3.1. Vanadium

During the early Cambrian Stage 3, a global transgression event contributed to the expansion of euxinic seawater, resulting in abnormally high trace element contents (Guo et al., 2016). For the Xa1 well, the V_{EF} is high in the LM shale (7.0–145.2), and moderate in the UM shale (1.5–4.6) (Figure 10A, Table 1). Similarly, the Xb1 well also exhibits relatively high V_{EF} in the LM-1 submember shale (5.2–18.3), moderate V_{EF} in the LM-2 submember shale (1.6–4.0), and low V_{EF} in the UM shale (1.1–2.5) (Figure 10C). The redox proxies suggest the water column of the LM and UM shales in the Xa1 well was persistently euxinic and with ferruginous conditions, while those of the LM-1, LM-2, and UM shales in the Xb1 well were intermittent euxinic, ferruginous, and suboxic, respectively (Figures 7 and 8). Vanadium is present as different valance states in oxic to anoxic conditions (Sadiq, 1988). Under oxic conditions, V exists as soluble HVO_4^{2-} and $H_2VO_4^-$ (V) in seawater, but is reduced to $VO(OH)_3^-$ (IV) or insoluble hydroxide (IV) and complexed by dissolved organic matter in seawater (Wehrli and Stumm, 1989; Scholz et al., 2011). Due to the large specific surface area of smectite, V-rich OM is then adsorbed or intercalated onto this clay mineral. When the reducibility of the water column is enhanced and free H_2S exists, V is further reduced to V_2O_3 or $V(OH)_3$ (III) (Breit and Wanty, 1991; Wanty and Goldhaber, 1992). Microscopic

observations suggest that vanadium is hosted in the Cambrian shale by organic matter, clay minerals, and the anatase, respectively (Figure 4). The complexation of organic matter and absorption of minerals played a critical role in the enrichment and redistribution of V in the black shale during the early Cambrian.

The V contents of the Niutitang shale in the Duoding and Longbiuzi sections also exhibit relatively high values at the bottom of the Niutitang shale, but low values in its upper part. Han et al (2018) suggested that dwindling concentrations of V and Zn in seawater existed in South China during the early Cambrian. This phenomenon should be the primary driver for this drawdown in the black shale, while redox condition and dissolved organic matter of seawater have little influence on it. However, the V content exhibits coupled patterns with Mo, U, and the Mo_{EF}/U_{EF} ratio in our study area (Figures 5, 6, 10), which suggest that euxinic conditions are more conducive to the enrichment of V than ferruginous and suboxic conditions. Furthermore, the distribution of the TOC and V contents in the Xa1 and Xb1 wells also indicate that the uptake capacity of dissolved organic matter in seawater for V through reduction and adsorption can improve the removal capacity of V scavenging in the seawater (Table 1). Then, V ions can replace Al ions in illite and Ti ions in anatase by isomorphism (Figure 4, Lu et al., 2021). Adsorption of clay minerals and mineral isomorphism also play important roles in the removal of V from seawater. This raises the question to why the geochemical behavior of V element in the Longbizui and Duoding sections and our study area seem contradictory? The iron speciation data suggest that the water columns in the Longbizui and Duoding sections were mainly suboxic to ferruginous environments (Wang et al., 2012; Jin et al., 2016). The difference of V enrichment in ferruginous and euxinic environments has been well-characterized in our study area. The depositional period of the LM shale in the Longbizui and Duoding sections was mainly from 521–518 Ma (Figure 2) at which time the drawdown of the element V in seawater occurred across South China (see above). In conclusion, the V inventory in the ocean, redox condition, organic matter, and clay minerals may jointly affect the enrichment of V in the black shale during the early Cambrian.

320

321 5.3.2. Zinc

322 In the Xa1 well, Zn_{EF} is high in the LM shale (1.4–210.0), but low in the UM shale
323 (0.3–1.2, Figure 10B). Similarly, the Xb1 well exhibits relatively high Zn_{EF} values in
324 the LM-1 submember shale (1.8–13.4), moderate values in the LM-2 submember shale
325 (1.4–3.7), and low values in the UM shale (1.4–1.9, Figure 10D). Zinc is present as
326 Zn^{2+} under oxic/suboxic conditions, while it precipitates rapidly in the form of ZnS
327 under anoxic conditions (Brumsack, 1989; Morse and Luther Iii, 1999). Sulfate
328 reducing bacteria can release Zn from organometallic complexes that can be absorbed
329 by adjacent authigenic sulfides (Fleurance et al., 2013; Slack et al., 2015). The Zn
330 content also exhibits coupled patterns with Mo, U, Mo_{EF}/U_{EF} ratio, and TOC content in
331 the Xa1 and Xb1 wells (Figures 5, 6, 9), which may be attributed to the redox condition
332 and dissolved organic matter. There are two different authigenic enrichment
333 mechanisms of Zn in modern and ancient oceans, termed primary and secondary
334 authigenic enrichment (Scott et al., 2017; Wang et al., 2020b). Primary enrichment is
335 related to H_2S in pore waters, and results in relatively low Zn content. Secondary
336 enrichment requires excess H_2S content, affects the activity phototrophic sulfide-
337 oxidizing bacteria, and results in "hyper-enrichment" of Zn (Overmann et al., 1996;
338 Findlay et al., 2014). The Zn content of the LM-1 submember shale in the Xb1 well and
339 the LM shale in the Xa1 well is abnormally high, which may be related to the free H_2S
340 in the paleo-ocean (Scott et al., 2017). Interestingly, the Zn content of the UM shale in
341 the Xa1 well was in a deficit state ($Zn_{EF}<1$), while that in the Xb1 well was slightly
342 enriched ($Zn_{EF}>1$, Table 1). The Zn content shows coupled patterns with V content in
343 the Niutitang shale (Figures 5, 6). Collectively this information indicates that the Zn
344 inventory in the ocean was similar to the V inventory, both of which were in a
345 downward trend. The drawdown of trace elements in seawater may provide an early-
346 stage preparation of the marine environment for the subsequent Chengjiang Biota (Han
347 et al., 2018).

348

5.4. Indicative significance of V and Zn anomalies during the early Cambrian

To address the question when did the V and Zn content of seawater decline in South China during the early Cambrian, we have collected trace element data from another seven sections in South China (Figure 11). The V and Zn content of the UM shale remains almost unchanged (Figures 11A, 11C), while those of the LM shale show large differences from the inner shelf to the basin facies (Figures 11B, 11D). Euxinic conditions are more favorable for the enrichment of trace elements (Figure 8). The LM shale with anomalously high V content firstly appeared in the outer shelf facies (Xy1 well and Jinsha section), while the samples with anomalously high Zn content appeared in the slope facies (Xb1 well). In terms of its sensitivity to redox changes, V is more redox-sensitive than Zn and removed earlier from seawater to sediments (Algeo and Maynard, 2004, 2008). Although the V content of the LM shale is abnormally high, there are also 20 samples with low V content in the LM shale (Figures 5, 6). The Zn contents of these samples are relatively low, and the Mo/TOC values are less than 10 (avg. 6), which is close to the values from the modern Black Sea (Algeo and Lyons, 2006; Algeo and Rowe, 2012). There is no difference in TOC content, redox condition, and seawater restriction between the samples with low V and anomalously high V content (Figures 5, 6, 10). The complexation of organic matter and absorption of clay minerals may remove the trace elements from seawater to sediment rapidly during the euxinic condition (Lu et al., 2021). We suggest that the samples with low trace element contents may be affected by dwindling seawater trace element inventory (Han et al., 2018). Considering how the shale samples with high content of V and Zn formed during this critical period, we suggest that the high trace element contents in the ocean would have had to be supplemented from other sources.

Hydrothermal activity in South China at 521 Ma is evidenced by intermittently distributed Ni-Mo ore layers developed at the bottom of the LM shale (Xu et al., 2011; Fan et al., 2020). The ocean was affected by multiple phases of hydrothermal activity during the depositional period of the LM shale (Chen et al., 2009; Fan et al., 2013; Liu et al., 2015; Gao et al., 2018). Hydrothermal activity strongly affected the marine

environment during this time interval, including enrichment of the toxic element mercury (Zhu et al., 2021), formation of chert and siliceous shale (Liu et al., 2015; Xie et al., 2021), and causing organismal extinctions (Wang et al., 2020b). Hyalophane minerals are present at different depths in the Xa1 and Xb1 wells. The formation mechanism of hyalophane can be divided into two types: metasomatism of authigenic barite, and crystallization of Ba-Al-Si colloid (McSwiggen et al., 1994; Raith et al., 2014). Barite minerals are rare and do not exhibit obvious metasomatic residual structure in our study areas (Figure 3). The formation of Ba-Al-Si colloids is generally related to hydrothermal action (Jacobsen et al., 1990; Moro et al., 2001), which can release large amounts of Ba and SiO_2 into seawater and precipitate to form siliceous colloids in the reducing environment. The anoxic environment in the study area also favors the formation of Ba-Al-Si colloids. The hyalophane mineral can therefore be an important indicator of hydrothermal activity (Figure 5). Furthermore, Zn is an important biological nutrient. The TM/C ratio (Zn=0.036 mmol/mol) of phytoplankton can be used to calculate the biological contribution to Zn content in sediment (Little et al., 2015). The TOC content of the LM shale is < 20% and the calculated biological contribution to Zn content is only 40 ppm. As the Zn content of the LM shale generally exceeds 500 ppm and can extend up to 5672 ppm, it shows that the contribution from organisms is negligible. Furthermore, the Zn content of the UM shale in the Xa1 well was in a deficit state (Zn_{EF}<1), while that in the Xb1 well was slightly enriched (Zn_{EF}>1). Due to the redox condition (Table 1), an oxic condition in the Xb1 well is more conducive to the blooming of phytoplankton, and the biological contribution to Zn content should be relatively higher. Fan et al. (2020) also analyzed Zn isotopes in the Ni-Mo layer, and suggested that hydrothermal activity provided another Zn source. The Ni-Mo layer developed at 521 Ma is also rich in V where its content varies between 0.5–1.2%, with this concentration reaching the industrial mining grade (Zhou et al., 2020). Hydrothermal fluids may have carried abundant trace element (V, Zn, and Ba) into the ocean during the depositional period of the LM shale, forming shales with anomalously high trace elements content in the euxinic environment (Figure 8).

Furthermore, the samples with high Zn content are also characterized by high V content (Figures 5, 6). There seems to be little correlation between V content and Zn content in the LM shale (Figure 12A). Here, we have selected the samples with high Zn and V contents, and found that the correlation between Zn and V content is strong in the LM shale ($n = 22$, $p < 0.01$, $r = 0.79$, Figure 12B). The above suggests that the trace element contents of seawater were intermittently supplied by hydrothermal activity, which strongly affected the enrichment of V and Zn elements.

5.5. Depositional environment and biological evolution from 521–514 Ma

The marine environment was significantly different during the depositional periods of the UM and LM shales, affected by redox condition, seawater restriction, hydrothermal activity, and the trace element inventory of seawater (Figure 13).

During the depositional period of the LM shale, the paleo-ocean presented a "euxinic wedge" model (Figure 13B), with the surface, middle, and deep ocean layers characterized by oxic, euxinic, and ferruginous conditions, respectively (Li et al., 2015; 2020). Free H_2S content was abundant in the seawater, and photic zone euxinia may have occurred in the slope-basin facies zone (Wang et al., 2020b). The shallow-water areas mainly experienced suboxic conditions, while the deep-water areas were persistently euxinic with intermittent ferruginous conditions (Figure 8). The ocean was also affected by multiple phases of hydrothermal activity during this period (Chen et al., 2009; Gao et al., 2018; Xie et al., 2021; Zhu et al., 2021). There existed a relatively high availability of fluvial Fe–Mn oxides and their subsequent reduction below the chemocline in the shallow-water areas (Cheng et al., 2016). The Mo/TOC ratio in the study area is close to present-day value of the Black Sea, indicating a strongly to moderately restricted condition. The V enrichment started at the suboxic-euxinic threshold, while Zn enrichment requires a more euxinic environment. Although the trace elements of seawater were in a dwindling state, episodic hydrothermal activities may have carried abundant trace elements (V, Zn, and Ba) into the ocean. V element is usually complexed by dissolved organic matter in seawater during the depositional

period. Due to the large specific surface area of smectite, the clay mineral then adsorbed or intercalated this V-rich OM (Lu et al., 2021). During pyrolysis of source rocks, the element V can be released from the organic matter and incorporated into the lattice of illite (conversion of smectite to illite mineral) and the mineral anatase, allowing V ions to replace Al ions in illite and Ti ions in anatase through isomorphism (Figure 4). Thus, the uptake of organic matter, and mineral isomorphism played critical roles in the enrichment and redistribution of V in the black shale during diagenesis. The element Zn is also associated with the adsorption of dissolved organic matter, and present as sphalerite in anoxic environments (Figure 3). The euxinic condition, organic matter, clay minerals, and sufficient trace element inventory were conducive to V and Zn enrichment. Oxic environments firstly appeared in the shallow-water areas during the late LM shale depositional period (Figure 8). Furthermore, the TOC content in the LM shale is higher than that in the UM shale. Previous studies suggest that the introduction of nutrient elements into the ocean via continental weathering and hydrothermal activity would lead to the blooming of phytoplankton (Gao et al., 2016; 2021; Xie et al., 2021). This should be considered as one of the main factors for organic matter enrichment in the Niutitang black shale.

During the depositional period of the UM shale, the surface layer in the ocean was in an oxic condition, and the middle and deep layers were in a ferruginous condition (Figure 13A). Oxic seawater gradually spread from the inner shelf to deeper basin settings (Figure 8). The Mo/TOC ratios of the UM shale suggest the marine environment was weakly restricted. Due to the cessation of hydrothermal activity and uptake of organic matter and clay minerals, the seawater trace element abundance was relatively low during the 518–514Ma interval. The TOC content of the UM shale was also lower than that of the LM shale. The enrichment of V and Zn in the UM shale was controlled by suboxic/ferruginous conditions, weakly restricted seawater, and dwindling trace element inventory of seawater. Expansion of oxic conditions and the introduction of nutrient elements may have provided an early-stage preparation of the marine environments for the subsequent Chengjiang/Qingjiang Biota.

6. Conclusions

Based on the analysis of lithofacies, mineralogy, and inorganic geochemistry of two wells in our study area and another seven sections from the inner shelf to basin facies in South China, we have elucidated the effects of redox condition, trace element contents of seawater and hydrothermal activity on the enrichment mechanisms for V and Zn during the early Cambrian. The V-rich hosts are mainly organic matter, illite, and anatase minerals, while the Zn-rich minerals are primarily sphalerite. Complexation of dissolved organic matter and adsorption of minerals should be the main ways to remove trace elements form seawater to sediments. In addition, the euxinic environment is more conducive to V and Zn accumulation than ferruginous condition during the early Cambrian. Although the dwindling V and Zn concentration of seawater existed in South China, episodic hydrothermal activity carried other source into the ocean, resulting in the shale formation with relatively high trace element contents. Consequently, organic matter, clay minerals，redox state of the water column, and trace elements of seawater, jointly affected the enrichment and migration of V and Zn in the Niutitang shale.

Acknowledgements

This work was supported by the National Natural Science Foundation of China (41872151), and the Open Foundation of Cooperative Innovation Center of Unconventional Oil and Gas, Yangtze University (No. UOG2022-18). We thank Associate Editor Swapan Kumar Sahoo, Thomas Algeo, Ping Gao and another anonymous reviewer for constructive comments on earlier versions of the manuscript.

References

Adelson, J., Helz, G., Miller, C., 2001. Reconstructing the rise of recent coastal anoxia; molybdenum in Chesapeake Bay sediments. Geochimica et Cosmochimica Acta 65, 237–252.

Algeo, T.J., Li, C., 2020. Redox classification and calibration of redox thresholds in sedimentary systems. Geochimica et Cosmochimica Acta 287, 8–26.

Algeo, T.J., Liu, J., 2020. A re-assessment of elemental proxies for paleoredox analysis. Chemical Geology 540, 119549.

Algeo, T.J., Lyons, T.W., 2006. Mo–total organic carbon covariation in modern anoxic marine environments: Implications for analysis of paleoredox and paleohydrographic conditions. Paleoceanography 21, 1016.

Algeo, T.J., Maynard, J.B., 2004. Trace-element behavior and redox facies in core shales of Upper Pennsylvanian Kansas-type cyclothems. Chemical Geology 206, 289–318.

Algeo, T.J., Maynard, J.B., 2008. Trace-metal covariation as a guide to water-mass conditions in ancient anoxic marine environments. Geosphere, 4, 872–887.

Algeo, T.J., Rowe, H., 2012. Paleoceanographic applications of trace-metal concentration data. Chemical Geology 324–325, 6–18.

Algeo, T.J., Tribovillard, N., 2009. Environmental analysis of paleoceanographic systems based on molybdenum–uranium covariation. Chemical Geology 268, 211–225.

Breit, G.N., Wanty, R.B., 1991. Vanadium accumulation in carbonaceous rocks: A review of geochemical controls during deposition and diagenesis. Chemical Geology 91, 83–97.

Brumsack, H.J., 1989. Geochemistry of recent TOC-rich sediments from the Gulf of California and the Black Sea. Geologische Rundschau 78, 851–882.

Canfield, D., 1998. A new model for Proterozoic ocean chemistry. Nature 396, 450–453.

Chen, D., Wang, J., Qing, H., Yan, D., Renwei, L.I., 2009. Hydrothermal venting activities in the Early Cambrian, South China: Petrological, geochronological and stable isotopic constraints. Chemical Geology 258, 168–181.

Chen, Z., Wang, G., Jin C., 2022. Marine redox variation and hydrographic restriction in the early Cambrian Nanhua Basin, South China. Palaeogeography, Palaeoclimatology, Palaeoecology 607, 111263.

Cheng, M., Li, C., Jin, C., Wang, H., Algeo, T.J., Lyons, T.W., Zhang, F., Anbar, A., 2020. Evidence for high organic carbon export to the early Cambrian seafloor. Geochimica et Cosmochimica Acta 287, 125–140.

Cheng, M., Li, C., Zhou, L., Algeo, T.J., Zhang, F., Romaniello, S., Jin, C., Lei, L., Feng, L., Jiang, S., 2016. Marine Mo biogeochemistry in the context of dynamically euxinic mid-depth waters: A case study of the lower Cambrian Niutitang shales, South China. Geochimica et Cosmochimica Acta 183, 79–93.

Coveney, R., Chen, N., 1991. Ni-Mo-PGE-Au-rich ores in Chinese black shales and speculations on possible analogues in the United States. Mineralium Deposita 26, 83–88.

Fan, H., Wen, H., Zhu, X., Hu, R., Tian, S., 2013. Hydrothermal activity during Ediacaran–Cambrian transition: Silicon isotopic evidence. Precambrian Research 224, 23–35.

Fan, H., Zhang, H., Xiao, C., Pašava, J., Han, T., Zhou, T., Wen, H., 2020. Large Zn isotope variations in the NiMo polymetallic sulfide layer in the lower Cambrian, South China. Gondwana Research 85, 224–236.

Feng, L., Li, C., Huang, J., Chang, H., Chu, X., 2014. A sulfate control on marine mid-depth euxinia on the early Cambrian (ca. 529–521 Ma) Yangtze platform, South China. Precambrian Research 246, 123–133.

Findlay, A.J., Gartman, A., MacDonald, D.J., Hanson, T.E., Shaw, T.J., Luther III, G.W., 2014. Distribution and size fractionation of elemental sulfur in aqueous environments: The Chesapeake Bay and Mid-Atlantic Ridge. Geochimica et Cosmochimica Acta 142, 334–348.

Fleurance, S., Cuney, M., Malartre, F., Reyx, J., 2013. Origin of the extreme polymetallic enrichment (Cd, Cr, Mo, Ni, U, V, Zn) of the Late Cretaceous–Early Tertiary Belqa Group, central Jordan. Palaeogeography, Palaeoclimatology, Palaeoecology 369, 201–219.

Gao, P., Liu, G., Jia, C., Young A., Wang, Z., Wang, T., Zhang, P., Wang, D., 2016. Redox variations and organic matter accumulation on the Yangtze carbonate platform during Late Ediacaran–Early Cambrian: Constraints from petrology and geochemistry. Palaeogeography, Palaeoclimatology, Palaeoecology, 450, 91–110.

Gao P., He Z., Lash G., Zhou, Q., Xiao, X., 2021. Controls on silica enrichment of lower Cambrian organic-rich shale deposits. Marine and petroleum Geology, 130, 105126.

Gao, P., He, Z., Li, S., Lash, G.G., Li, B., Huang, B., Yan, D., 2018. Volcanic and hydrothermal activities recorded in phosphate nodules from the Lower Cambrian Niutitang Formation black shales in South China. Palaeogeography, Palaeoclimatology, Palaeoecology 505, 381–397.

Gill, B.C., Lyons, T.W., Young, S.A., Kump, L.R., Knoll, A.H., Saltzman, M.R., 2011. Geochemical evidence for widespread euxinia in the Later Cambrian ocean. Nature 469, 80–83.

Goldberg, T., Strauss, H., Guo, Q., Liu, C., 2007. Reconstructing marine redox conditions for the Early Cambrian Yangtze Platform: Evidence from biogenic sulphur and organic carbon isotopes. Palaeogeography, Palaeoclimatology, Palaeoecology 254, 175–193.

Guo, Q., Deng, Y., Hippler, D., Franz, G., Zhang, J., 2016. REE and trace element patterns from organic-rich rocks of the Ediacaran–Cambrian transitional interval. Gondwana Research 36, 94–106.

Han, T., Fan, H., Wen, H., 2018. Dwindling vanadium in seawater during the early Cambrian, South China. Chemical Geology 492, 20–29.

Han, T., Fan, H., Wen, H., Mo, B., Murowchick, J.B., Lu, Z., Algeo, T.J., 2020. Petrography and sulfur isotopic compositions of SEDEX ores in the early Cambrian Nanhua Basin, South China. Precambrian Research 345, 105757.

Han, T., Fan, H., Zhu, X., Wen, H., Zhao, C., Xiao, F., 2017. Submarine hydrothermal contribution for the extreme element accumulation during the early Cambrian, South China. Ore Geology Reviews 86, 297–308.

Jakobsen, U. H. 1990. A hydrated barium silicate in unmetamorphosed sedimentary rocks of central North Greenland. Mineralogical Magazine, 374 81-89.

Jenkins, R., Cooper, J.A.a., Compston, W., 2002. Age and biostratigraphy of Early Cambrian tuffs from SE Australia and southern China. Journal of the Geological Society 159, 645–658.

Jiang, G., Wang, X., Shi, X., Xiao, S., Zhang, S., Dong, J., 2012. The origin of decoupled carbonate and organic carbon isotope signatures in the early Cambrian (ca. 542–520 Ma) Yangtze platform. Earth and Planetary Science Letters 317, 96–110.

Jiang, S.-Y., Chen, Y.-Q., Ling, H.-F., Yang, J.-H., Feng, H.-Z., Ni, P., 2006. Trace-and rare-earth element geochemistry and Pb–Pb dating of black shales and intercalated Ni–Mo–PGE–Au sulfide ores in Lower Cambrian strata, Yangtze Platform, South China. Mineralium Deposita 41, 453–467.

Jin, C., Li, C., Algeo, T.J., Planavsky, N.J., Cui, H., Yang, X., Zhao, Y., Zhang, X., Xie, S., 2016. A highly redox-heterogeneous ocean in South China during the early Cambrian (~529–514 Ma): Implications for biota-environment co-evolution. Earth and Planetary Science Letters 441, 38–51.

Jones, B., Manning, D.A., 1994. Comparison of geochemical indices used for the interpretation of palaeoredox conditions in ancient mudstones. Chemical geology 111, 111–129.

Li, C., Love, G.D., Lyons, T.W., Fike, D.A., Sessions, A.L., Chu, X., 2010. A stratified redox model for

584 the Ediacaran ocean. Science 328, 80–83.
585 Li, C., Cheng, M., Algeo, T.J., Xie, S., 2015. A theoretical prediction of chemical zonation in early oceans
586 (> 520 Ma). Science China Earth Sciences, 58, 1901–1909.Li, C., Shi, W., Cheng, M., Jin, C.,
587 Algeo, T.J., 2020. The redox structure of Ediacaran and early Cambrian oceans and its controls.
588 Science Bulletin, 65, 2141–2149.
589 Li, J., Tang, S., Zhang, S., Xi, Z., Yang, N., Yang, G., Li, L., Li, Y., 2018. Paleo-environmental conditions
590 of the Early Cambrian Niutitang Formation in the Fenggang area, the southwestern margin of
591 the Yangtze Platform, southern China: Evidence from major elements, trace elements and other
592 proxies. Journal of Asian Earth Sciences 159, 81–97.
593 Li, N., Li, C., Fan, J., Algeo, T.J., Yan, D., Zhu, G., Wu, S., Tang, S., Cheng, M., Jin, C., 2019. Sulfate-
594 controlled marine euxinia in the semi-restricted inner Yangtze Sea (South China) during the
595 Ordovician-Silurian transition. Palaeogeography, Palaeoclimatology, Palaeoecology 534,
596 109281.
597 Li, S., Gao, Z., 2000. Source tracing of noble metal elements in Lower Cambrian black rock series of
598 Guizhou-Hunan Provinces, China. Science in China Series D: Earth Sciences 43, 625–632.
599 Li, Z.X., Bogdanova, S.V., Collins, A.S., Davidson, A., De Waele, B., Ernst, R.E., Fitzsimons, I.C.W.,
600 Fuck, R.A., Gladkochub, D.P., Jacobs, J., Karlstrom, K.E., Lu, S., Natapov, L.M., Pease, V.,
601 Pisarevsky, S.A., Thrane, K., Vernikovsky, V., 2008. Assembly, configuration, and break-up
602 history of Rodinia: A synthesis. Precambrian Research 160, 179–210.
603 Little, S.H., Vance, D., Lyons, T.W., McManus, J., 2015. Controls on trace metal authigenic enrichment
604 in reducing sediments: insights from modern oxygen-deficient settings. American Journal of
605 Science 315, 77–119.
606 Liu, Z.H., Zhuang, X., Teng, G., Xie, X., Yin, L., Bian, L., Feng, Q., Algeo, T.J., 2015. Organic matter
607 enrichment and source rock potential of the lower Cambrian Niutitang Formation at Yangtiao,
608 Guizhou, SW China. Journal of Petroleum Geology, 38, 411–432.
609 Lu, Z., Hu, R., Han, T., Wen, H., Mo, B., Algeo, T.J., 2021. Control of V accumulation in organic-rich
610 shales by clay-organic nanocomposites. Chemical Geology, 567, 120100.
611 McLennan, S.M., 2001. Relationships between the trace element composition of sedimentary rocks and
612 upper continental crust. Geochemistry, Geophysics, Geosystems 2.
613 McSwiggen P. L., Morey G. B., Cleland J M., 1994. Occurrence and genetic implications of hyalophane
614 in manganese-rich iron-formation, Cuyuna Iron Range, Minnesota, USA. Mineralogical
615 Magazine, 58, 387–399.
616 Moro, M.C., Cembranos, M.L., Fernandez, A., 2001. Celsian, (Ba, K)-feldspar and cymrite from sedex
617 barite deposits of Zamora, Spain. The Canadian Mineralogist 39, 1039–1051.
618 Morse, J., Luther Iii, G., 1999. Chemical influences on trace metal-sulfide interactions in anoxic
619 sediments. Geochimica et Cosmochimica Acta 63, 3373–3378.
620 Och, L.M., Shields-Zhou, G.A., Poulton, S.W., Manning, C., Thirlwall, M.F., Li, D., Chen, X., Ling, H.,
621 Osborn, T., Cremonese, L., 2013. Redox changes in Early Cambrian black shales at Xiaotan
622 section, Yunnan Province, south China. Precambrian Research 225, 166–189.
623 Okada, Y., Sawaki, Y., Komiya, T., Hirata, T., Takahata, N., Sano, Y., Han, J., Maruyama, S., 2014. New
624 chronological constraints for Cryogenian to Cambrian rocks in the Three Gorges, Weng'an and
625 Chengjiang areas, South China. Gondwana Research 25, 1027–1044.
626 Overmann, J., Beatty, J.T., Krause, H.R., Hall, K.J., 1996. The sulfur cycle in the chemocline of a
627 meromictic salt lake. Limnology and oceanography 41, 147–156.

628 Paschall, O., Carmichael, S.K., Königshof, P., Waters, J.A., Ta, P.H., Komatsu, T., Dombrowski, A., 2019.
629 The Devonian-Carboniferous boundary in Vietnam: Sustained ocean anoxia with a volcanic
630 trigger for the Hangenberg Crisis? Global and Planetary Change 175, 64–81.
631 Poulton, S.W., Canfield, D.E., 2005. Development of a sequential extraction procedure for iron:
632 implications for iron partitioning in continentally derived particulates. Chemical geology 214,
633 209–221.
634 Raiswell, R., Buckley, F., Berner, R.A., Anderson, T., 1988. Degree of pyritization of iron as a
635 paleoenvironmental indicator of bottom-water oxygenation. Journal of Sedimentary Research
636 58, 812–819.
637 Raith M., Devaraju T., Spiering B., 2014. Paragenesis and chemical characteristics of the celsian
638 hyalophane−K-feldspar series and associated Ba-Cr micas in barite-bearing strata of the
639 Mesoarchaean Ghattihosahalli Belt, Western Dharwar Craton, South India. Mineralogy and
640 Petrology, 108, 153–176.
641 Sadiq, M., 1988. Thermodynamic solubility relationships of inorganic vanadium in the marine
642 environment. Marine Chemistry 23, 87–96.
643 Scholz, F., Hensen, C., Noffke, A., Rohde, A., Liebetrau, V., Wallmann, K., 2011. Early diagenesis of
644 redox-sensitive trace metals in the Peru upwelling area – response to ENSO-related oxygen
645 fluctuations in the water column. Geochimica et Cosmochimica Acta 75, 7257–7276.
646 Scott, C., Lyons, T.W., 2012. Contrasting molybdenum cycling and isotopic properties in euxinic versus
647 non-euxinic sediments and sedimentary rocks: Refining the paleoproxies. Chemical Geology
648 324, 19–27.
649 Scott, C., Slack, J.F., Kelley, K.D., 2017. The hyper-enrichment of V and Zn in black shales of the Late
650 Devonian-Early Mississippian Bakken Formation (USA). Chemical Geology 452, 24–33.
651 Slack, J.F., Selby, D., Dumoulin, J.A., 2015. Hydrothermal, biogenic, and seawater components in
652 metalliferous black shales of the Brooks Range, Alaska: synsedimentary metal enrichment in a
653 carbonate ramp setting. Economic Geology 110, 653–675.
654 Tan, J., Wang, Z., Wang, W., Hilton, J., Guo, J., Wang, X., 2021. Depositional environment and
655 hydrothermal controls on organic matter enrichment in the lower Cambrian Niutitang shale,
656 southern China. AAPG Bulletin 105, 1329–1356.
657 Taylor, S.R., McLennan, S.M., 1995. The geochemical evolution of the continental crust. Reviews of
658 geophysics 33, 241–265.
659 Tourtelot, H.A., 1979. Black shale—its deposition and diagenesis. Clays and clay minerals 27, 313-321.
660 Tribovillard, N., Algeo, T.J., Baudin, F., Riboulleau, A., 2012. Analysis of marine environmental
661 conditions based onmolybdenum–uranium covariation—Applications to Mesozoic
662 paleoceanography. Chemical Geology 324, 46–58.
663 Tribovillard, N., Algeo, T.J., Lyons, T., Riboulleau, A., 2006. Trace metals as paleoredox and
664 paleoproductivity proxies: An update. Chemical Geology 232, 12–32.
665 Wang, J., Chen, D., Yan, D., Wei, H., Xiang, L., 2012. Evolution from an anoxic to oxic deep ocean
666 during the Ediacaran–Cambrian transition and implications for bioradiation. Chemical Geology
667 306-307, 129–138.
668 Wang, Z., Tan, J., Boyle, R., Hilton, J., Ma, Z., Wang, W., Lyu, Q., Kang, X., Luo, W., 2020a. Evaluating
669 episodic hydrothermal activity in South China during the early Cambrian: Implications for
670 biotic evolution. Marine and Petroleum Geology 117, 104355.
671 Wang, Z., Tan, J., Boyle, R., Wang, W., Kang, X., Dick, J., Lyu, Q., 2020b. Mercury anomalies within

the lower Cambrian (stage 2–3) in South China: Links between volcanic events and paleoecology. Palaeogeography, Palaeoclimatology, Palaeoecology 558, 109956.

Wanty, R.B., Goldhaber, M.B., 1992. Thermodynamics and kinetics of reactions involving vanadium in natural systems: Accumulation of vanadium in sedimentary rocks. Geochimica et Cosmochimica Acta 56, 1471–1483.

Wehrli, B., Stumm, W., 1989. Vanadyl in natural waters: Adsorption and hydrolysis promote oxygenation. Geochimica et Cosmochimica Acta 53, 69–77.

Wen, H., Fan, H., Zhang, Y., Cloquet, C., Carignan, J., 2015. Reconstruction of early Cambrian ocean chemistry from Mo isotopes. Geochimica et Cosmochimica Acta 164, 1–16.

Xiang, L., Schoepfer, S.D., Shen, S.-z., Cao, C.-q., Zhang, H., 2017. Evolution of oceanic molybdenum and uranium reservoir size around the Ediacaran–Cambrian transition: evidence from western Zhejiang, South China. Earth and Planetary Science Letters 464, 84–94.

Xie, X., Zhu, G., Wang, Y., 2021. The influence of syngenetic hydrothermal silica fluid on organic matter preservation in lower Cambrian Niutitang Formation, South China. Marine and Petroleum Geology 129, 105098.

Xu, L., Lehmann, B., Mao, J., Qu, W., Du, A., 2011. Re-Os age of polymetallic Ni-Mo-PGE-Au mineralization in Early Cambrian black shales of South China—a reassessment. Economic Geology 106, 511–522.

Yang, A., Zhu, M., Zhang, J., Li, G., 2003. Early Cambrian eodiscoid trilobites of the Yangtze Platform and their stratigraphic implications. Progress in Natural Science 13, 861–866.

Yang, C., Li, X.-H., Zhu, M., Condon, D.J., Chen, J., 2018. Geochronological constraint on the Cambrian Chengjiang biota, South China. Journal of the Geological Society 175, 659–666.

You, C.-F., Castillo, P., Gieskes, J., Chan, L., Spivack, A., 1996. Trace element behavior in hydrothermal experiments: Implications for fluid processes at shallow depths in subduction zones. Earth and Planetary Science Letters 140, 41–52.

Zhao, J., Jin, Z., Jin, Z., Geng, Y., Wen, X., Yan, C., 2016. Applying sedimentary geochemical proxies for paleoenvironment interpretation of organic-rich shale deposition in the Sichuan Basin, China. International Journal of Coal Geology 163, 52–71.

Zhou, Y., Ling, L., Wen, C., Mi, W., Zhu, L., Zhu, K., Yang, W., Pang, Y., 2020. Study on the occurrence state of Ni-Mo-V from the polymetallic layers in Niutitang Formation, Weng'an County, Guizhou. Mineralogy and Petrology 40, 67–81(In Chinese with English Abstract).

Zhu, G., Zhao, K., Li, T., Zhang, Z., Tang, S., Wang, P., 2021. Anomalously high enrichment of mercury in early Cambrian black shales in South China. Journal of Asian Earth Sciences 216, 104794.

Zou, C., Qiu, Z., Poulton, S.W., Dong, D., Wang, H., Chen, D., Lu, B., Shi, Z., Tao, H., 2018. Ocean euxinia and climate change “double whammy” drove the Late Ordovician mass extinction. Geology 46, 535–538.

Figures and Tables

Figure 1. Paleogeographic maps of the Yangtze Block during the late Ediacaran and early Cambrian. (A) Latest Ediacaran to earliest Cambrian Fortunian Stage (539 Ma, modified after Jiang et al. (2012). (B) Early Cambrian Stage 3 (521 Ma). (C) Depth and relative position of the nine studied early Cambrian Stage 3 period sections in South China.

Figure 2 Stratigraphic correlation with biostratigraphic dating of lower Cambrian (Ca. 539–514 Ma) sections across South China. Data sources: 1-Meishucun section, Yunnan Province (Jenkins et al., 2002; Yang et al., 2003; Wen et al., 2015); 2-Xiaotan section, Yunnan Province (Och et al., 2013); 3-Jinsha section, Guizhou Province (Jin et al., 2016); 4-Xy1 well, Guizhou Province (Li et al., 2018); 5-Yangjiaping section, Hunan Province (Cheng et al., 2016); 6-Xb1 well, Hunan Province (this study); 7-Longbizui section, Hunan Province (Wang et al., 2012); 8-Yuanjia section, Hunan Province (Cheng et al., 2020); and 9-Xa1 well, Hunan Province (this study). SSF: small shelly fossil assemblages, LCP: Liuchapo Formation, DY: Dengying Formation, CLP: Canglangpu Formation, MXS: Mingxinsi Formation, LM: lower member of the Niutitang/Yu'anshan Formation, UM: upper member of the Niutitang/Yu'anshan Formation.

Figure 3 Petrographic observations of studied samples in the Xa1 and Xb1 wells by scanning electron microscopy. (A) Pyrite (depth 843.3m, Xa1 well); (B) Celsian, hyalophane and pyrite (depth 849.8m, Xa1 well); (C) Celsian, monazite and pyrite (depth 849.8m, Xa1 well); (D) Celsian, barite and pyrite (depth 856.4m, Xa1 well); (E) Barite and pyrite (depth 2002.0m, Xb1 well); (F) Celsian (depth 2012.0m, Xb1 well); (G) Hyalophane and rutile (depth 2015.0m, Xb1 well); (H) Sphalerite and pyrite (depth 2018.0m, Xb1 well); (I) Sphalerite, calcium carbonate and pyrite (depth 2020.0m, Xb1 well).

Figure 4. Petrographic observations of V-rich shale samples in the Xa1 and Xb1 wells by scanning electron microscopy. (A) Anatase, organic matter and celsian (depth 849.8m, Xa1 well); (B) Anatase, celsian and hyalophane (depth 2010.5m, Xb1 well); (C) Anatase and calcium phosphate (depth 2013.2m, Xb1 well); (D) V concentration in organic matter, anatase, and illite minerals of A and B; (E) Anatase and Hyalophane (depth 855.2m, Xa1 well); (F) Anatase, pyrite and monazite (depth 2017.0m, Xb1 well).

Figure 5 Distribution of Mo, U, V, Zn, TOC content, Mo_{EF}/U_{EF}, and Mo/TOC ratios of the Niutitang Formation at the Xa1 well, Hunan Province.

Figure 6 Distribution of Mo, U, V, Zn, TOC content, Mo_{EF}/U_{EF}, and Mo/TOC ratios of the Niutitang Formation at the Xb1 well, Hunan Province.

Figure 7 The Mo enrichment factor (Mo_{EF}) versus U enrichment factor (U_{EF}) plot in the Xa1 (A) and Xb1 wells (B).

Figure 8 Spatio-temporal variations of redox conditions from the inner shelf to basin facies.

Figure 9 Mo concentrations versus total organic carbon (TOC) contents in the UM shale (A) and LM shale (B). Dashed lines represent four modern anoxic basin systems in the Saanich Inlet, Cariaco Basin, Framvaren Fjord, and Black Sea (Algeo and Lyons, 2006), showing different seawater restriction environments.

Figure 10 Mo_{EF}/U_{EF} versus V_{EF} (A) and Zn_{EF} (B) in the Xa1 well, Mo_{EF}/U_{EF} versus V_{EF} (C) and Zn_{EF} (D) in the Xb1 well.

Figure 11 TOC content versus V content (A) and Zn content (C) in the UM shale,

767 TOC content versus V content (B) and Zn content (D) in the LM shale.

768

769 **Figure 12** Zn content versus V content in LM shale (A); Zn content versus V content

770 in LM shale with abnormally high Zn content.

771

772 **Figure 13** Depositional models and inferred geochemical cycle of V and Zn in the early

773 Cambrian paleo-ocean in South China.

774

775

776 **Table 1** Redox condition, TOC content, Mo/TOC ratio, V_{EF} and Zn_{EF} of Niutitang

777 shale in Xa1 well and Xb1 well.

778

779

Figure 1

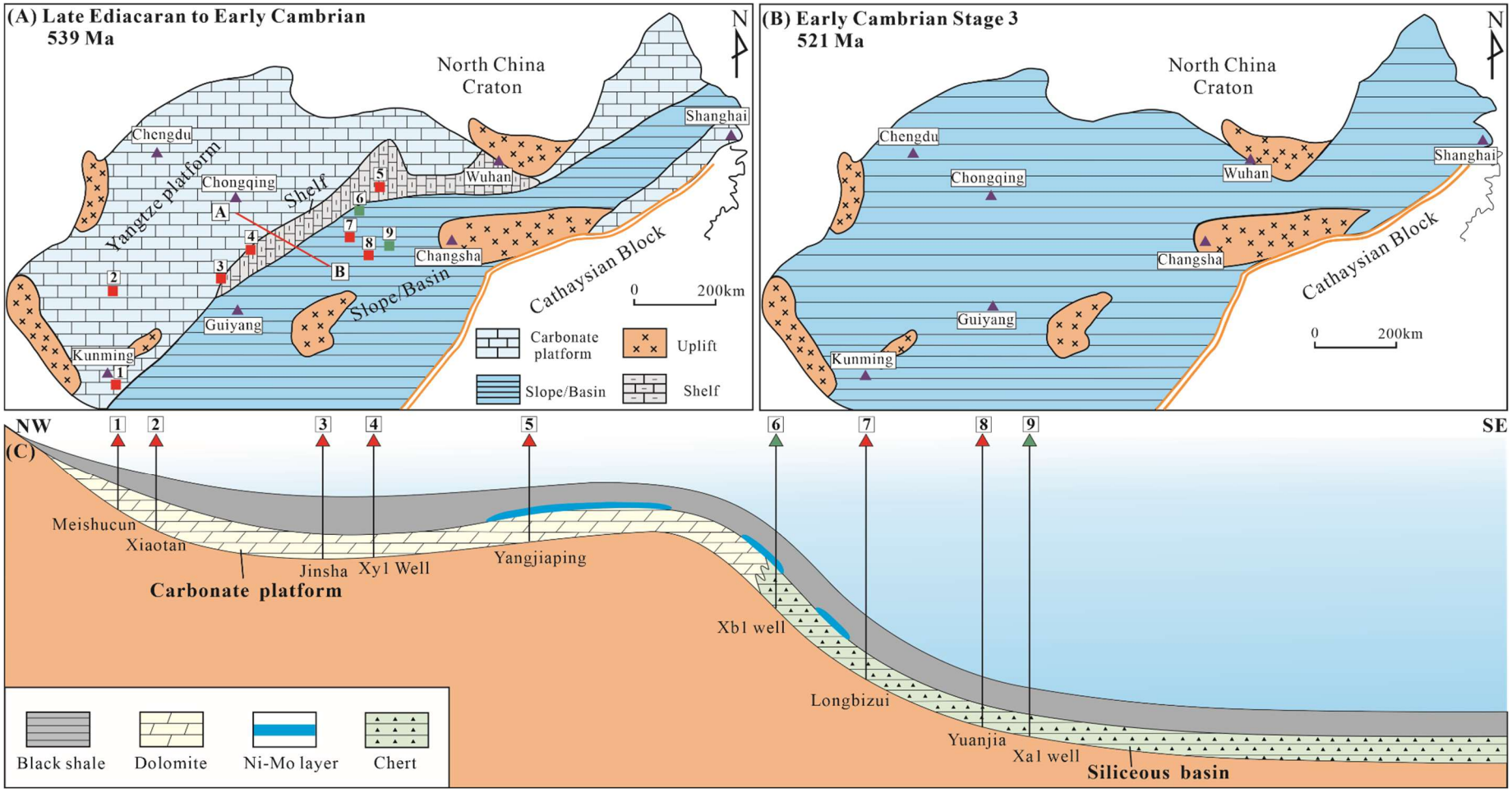
(A) Late Ediacaran to Early Cambrian
539 Ma
North China Craton
Chengdu
Chongqing
Wuhan
Shanghai
Changsha
Guiyang
Kunming
Yangtze platform
Shelf
Slope/Basin
Cathaysian Block
A
B
1
2
3
4
5
6
7
8
9
0
200km
Carbonate platform
Uplift
Slope/Basin
Shelf
N
(B) Early Cambrian Stage 3
521 Ma
North China Craton
Chengdu
Chongqing
Wuhan
Shanghai
Changsha
Guiyang
Kunming
Cathaysian Block
0
200km
N
NW
SE
(C)
Meishucun
Xiaotan
Jinsha
Xy1 Well
Yangjiaping
Carbonate platform
Xb1 well
Longbizui
Yuanjia
Xa1 well
Siliceous basin
Black shale
Dolomite
Ni-Mo layer
Chert

Figure 2

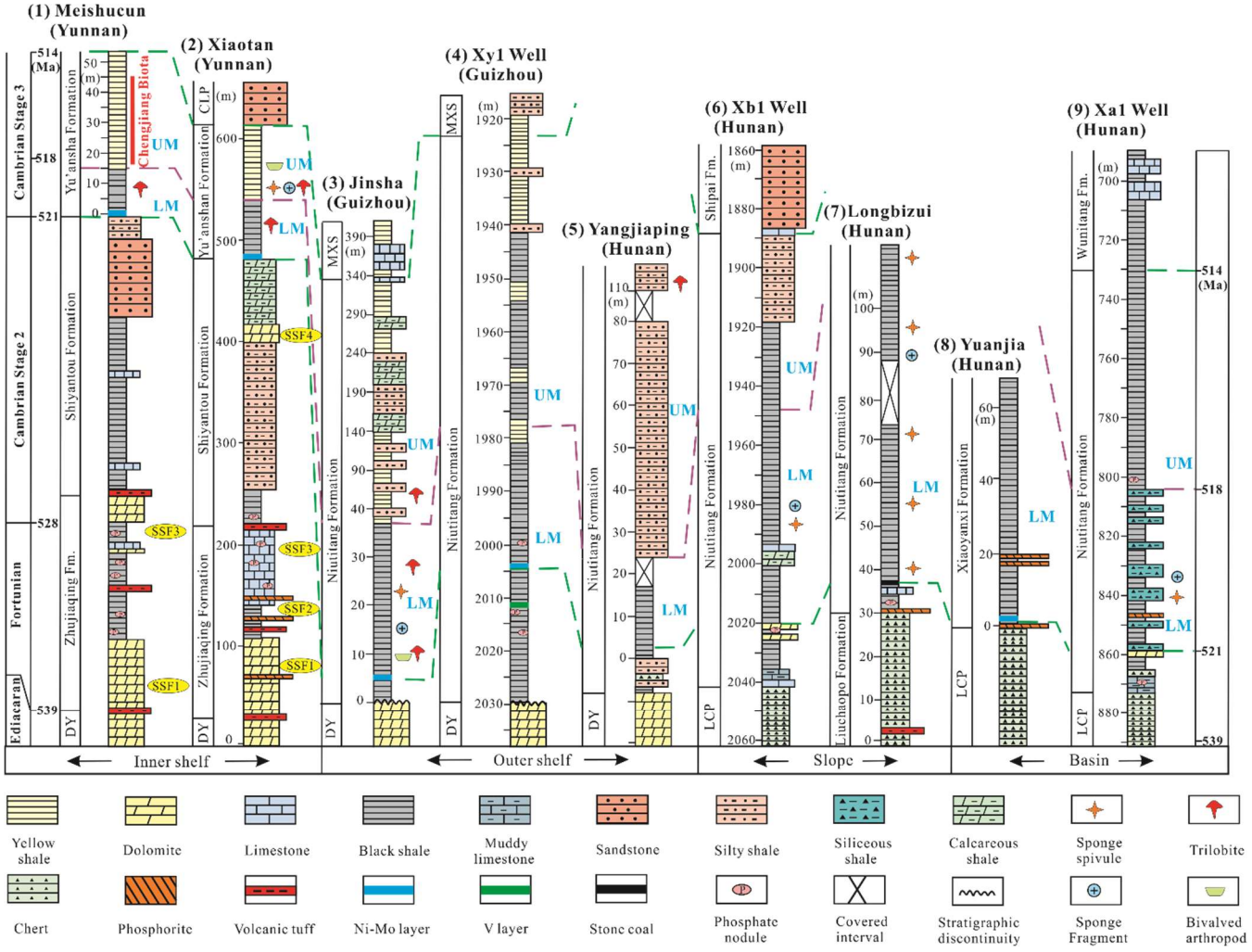
(1) Meishucun (Yunnan)
(2) Xiaotan (Yunnan)
(3) Jinsha (Guizhou)
(4) Xy1 Well (Guizhou)
(5) Yangjiaping (Hunan)
(6) Xb1 Well (Hunan)
(7) Longbizui (Hunan)
(8) Yuanjia (Hunan)
(9) Xa1 Well (Hunan)
Cambrian Stage 3
Cambrian Stage 2
Fortunian
Ediacaran
Yu'ansha Formation
Shiyantou Formation
Zhujiaqing Fm.
Zhujiaqing Formation
Chengjiang Biota
CLP
MXS
DY
Niutitang Formation
Shipai Fm.
Liuchapo Formation
Xiaoyanxi Formation
LCP
Wunitang Fm.
UM
LM
SSF1
SSF2
SSF3
SSF4
Inner shelf
Outer shelf
Slope
Basin
Yellow shale
Dolomite
Limestone
Black shale
Muddy limestone
Sandstone
Silty shale
Siliceous shale
Calcareous shale
Sponge spivule
Trilobite
Chert
Phosphorite
Volcanic tuff
Ni-Mo layer
V layer
Stone coal
Phosphate nodule
Covered interval
Stratigraphic discontinuity
Sponge Fragment
Bivalved arthropod

Figure 3

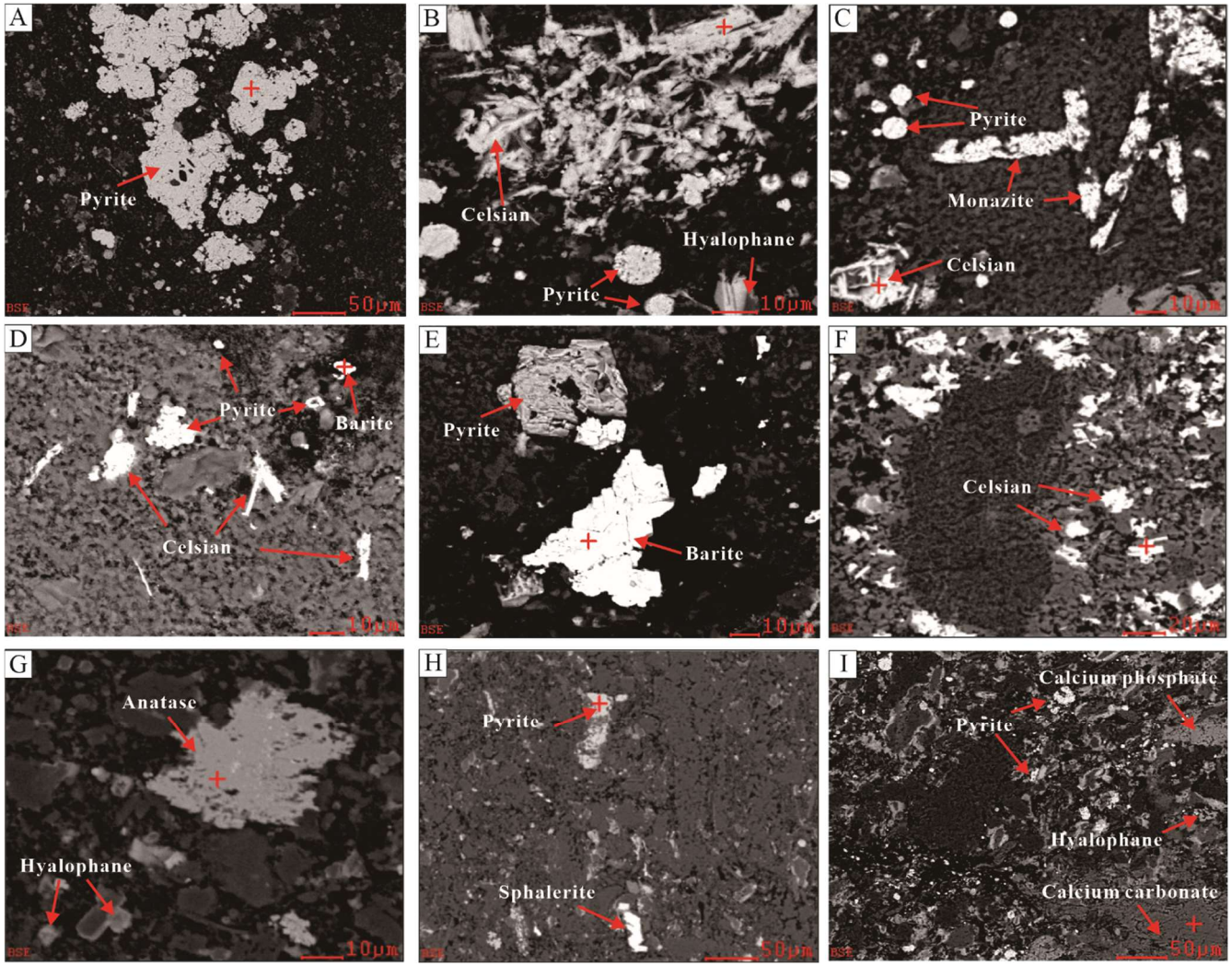
A
Pyrite
50μm
B
Celsian
Hyalophane
Pyrite
10μm
C
Pyrite
Monazite
Celsian
10μm
D
Pyrite
Barite
Celsian
10μm
E
Pyrite
Barite
10μm
F
Celsian
20μm
G
Anatase
Hyalophane
10μm
H
Pyrite
Sphalerite
50μm
I
Calcium phosphate
Pyrite
Hyalophane
Calcium carbonate
50μm

788 **Figure 4**

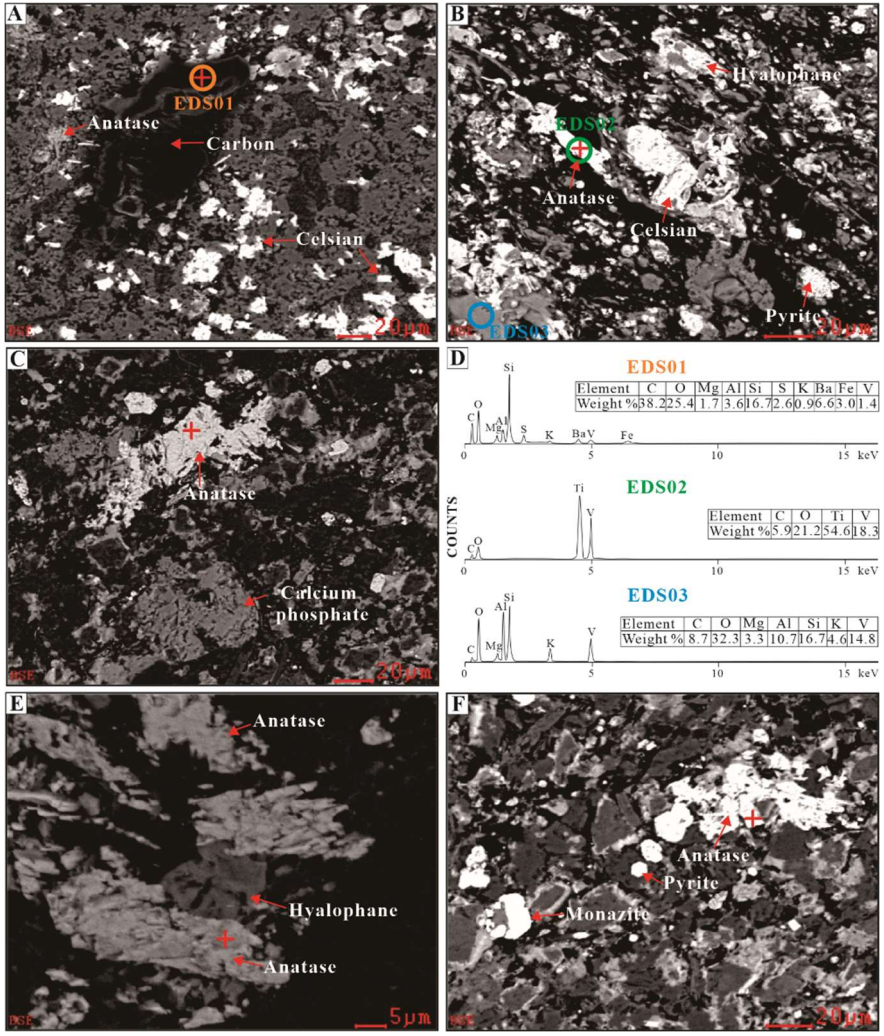

789

Figure 5

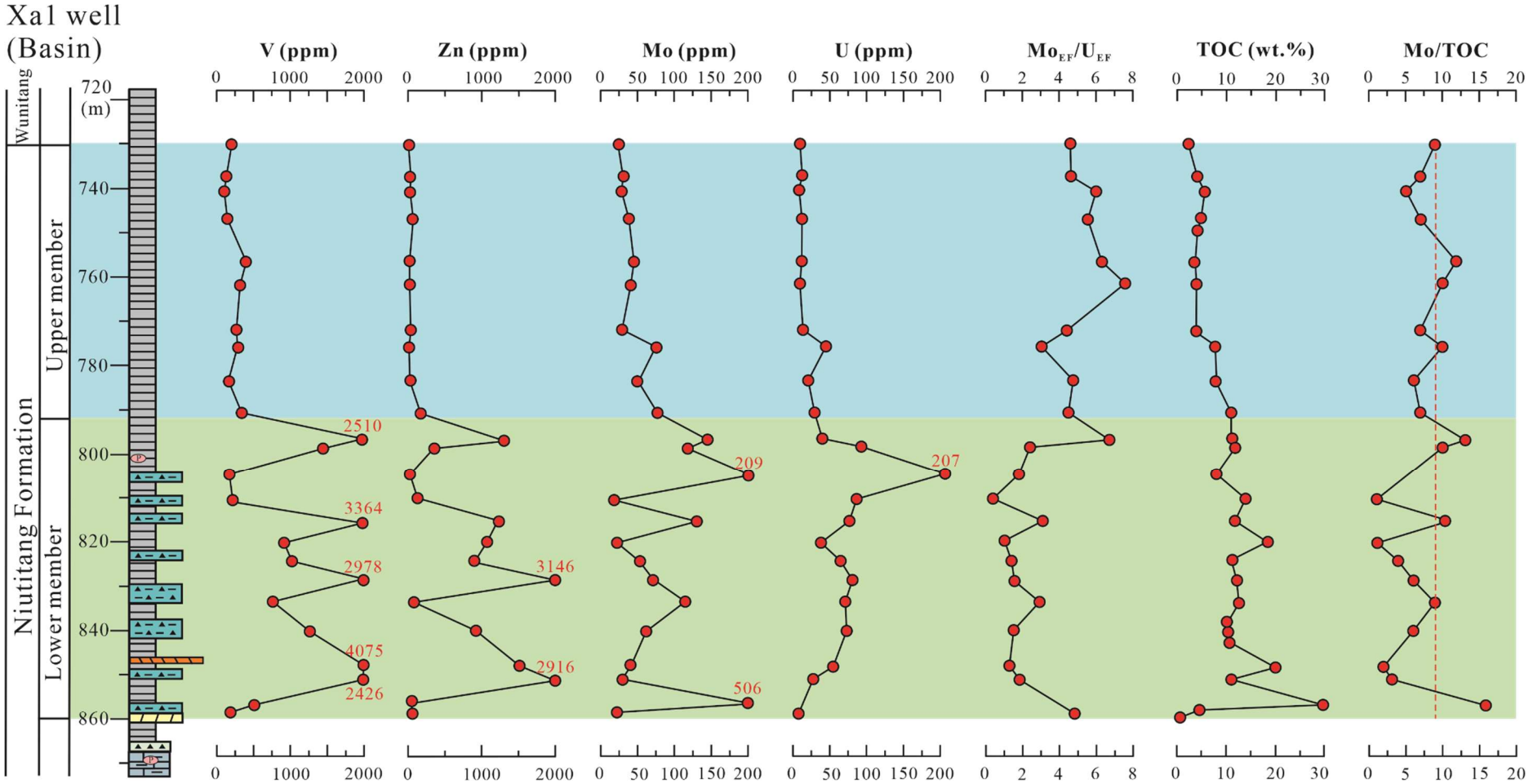
Xa1 well
(Basin)
V (ppm)
Zn (ppm)
Mo (ppm)
U (ppm)
Mo$_{EF}$/U$_{EF}$
TOC (wt.%)
Mo/TOC
Wunitang
Niutitang Formation
Upper member
Lower member
720
(m)
740
760
780
800
820
840
860
2510
3364
2978
4075
2426
3146
2916
209
506
207
0 1000 2000
0 50 100 150 200
0 2 4 6 8
0 10 20 30
0 5 10 15 20

Figure 6

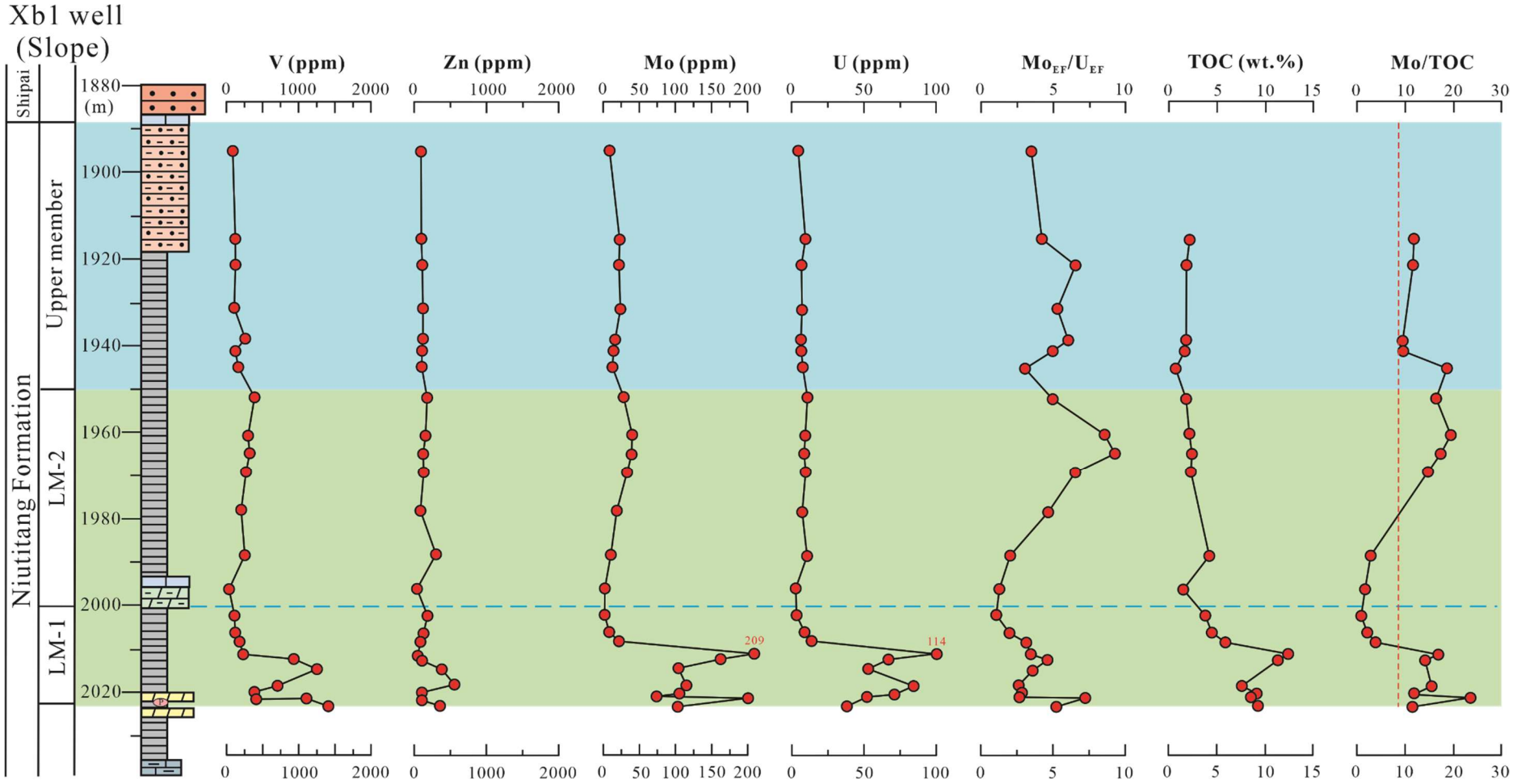
Xb1 well
(Slope)
Shipai
Niutitang Formation
Upper member
LM-2
LM-1
1880
(m)
1900
1920
1940
1960
1980
2000
2020
V (ppm)
Zn (ppm)
Mo (ppm)
U (ppm)
Mo_EF/U_EF
TOC (wt.%)
Mo/TOC
209
114

Figure 7

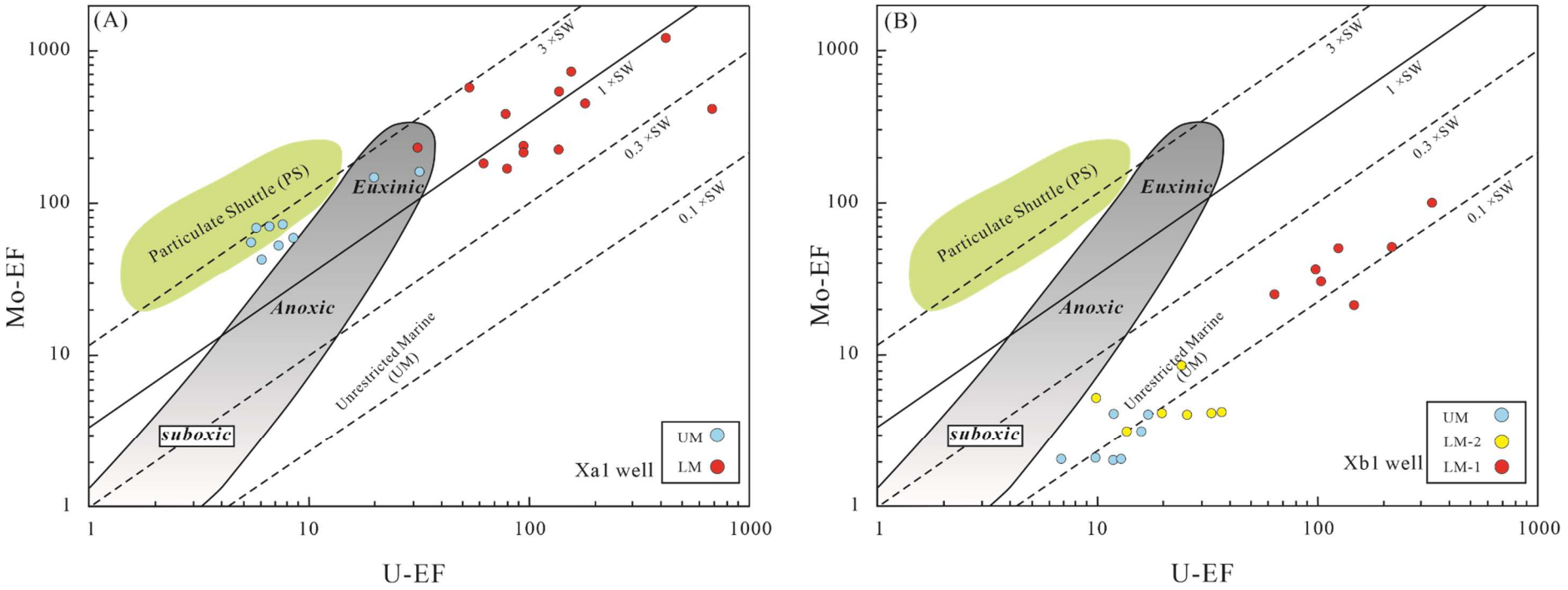
(A)
(B)
Mo-EF
U-EF
1000
100
10
1
1
10
100
1000
3 ×SW
1 ×SW
0.3 ×SW
0.1 ×SW
Particulate Shuttle (PS)
Euxinic
Anoxic
suboxic
Unrestricted Marine (UM)
Xa1 well
Xb1 well
UM
LM
LM-2
LM-1

Figure 8

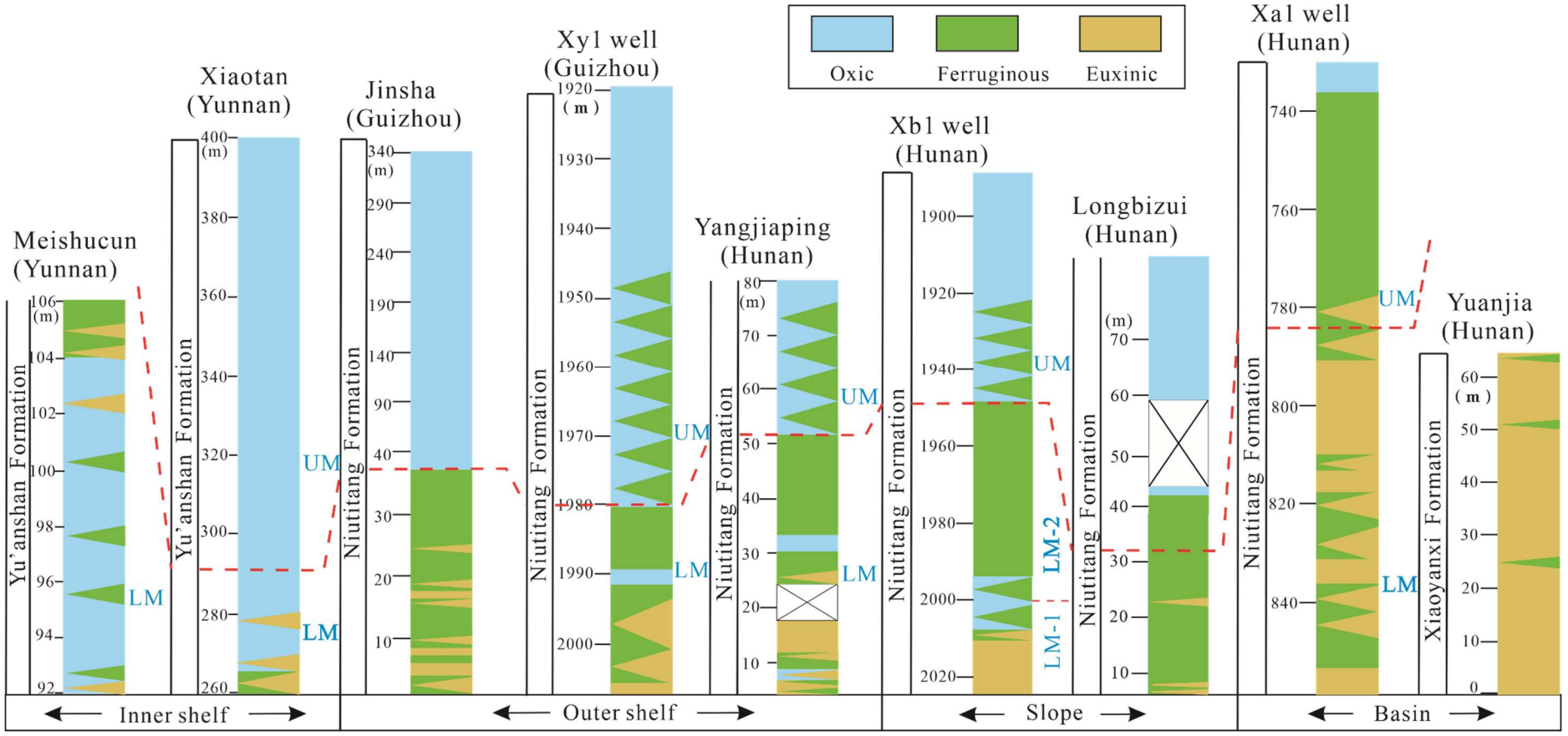
Oxic
Ferruginous
Euxinic
Meishucun (Yunnan)
Xiaotan (Yunnan)
Jinsha (Guizhou)
Xy1 well (Guizhou)
Yangjiaping (Hunan)
Xb1 well (Hunan)
Longbizui (Hunan)
Xa1 well (Hunan)
Yuanjia (Hunan)
Yu'anshan Formation
Niutitang Formation
Xiaoyanxi Formation
UM
LM
LM-1
LM-2
(m)
Inner shelf
Outer shelf
Slope
Basin

Figure 9

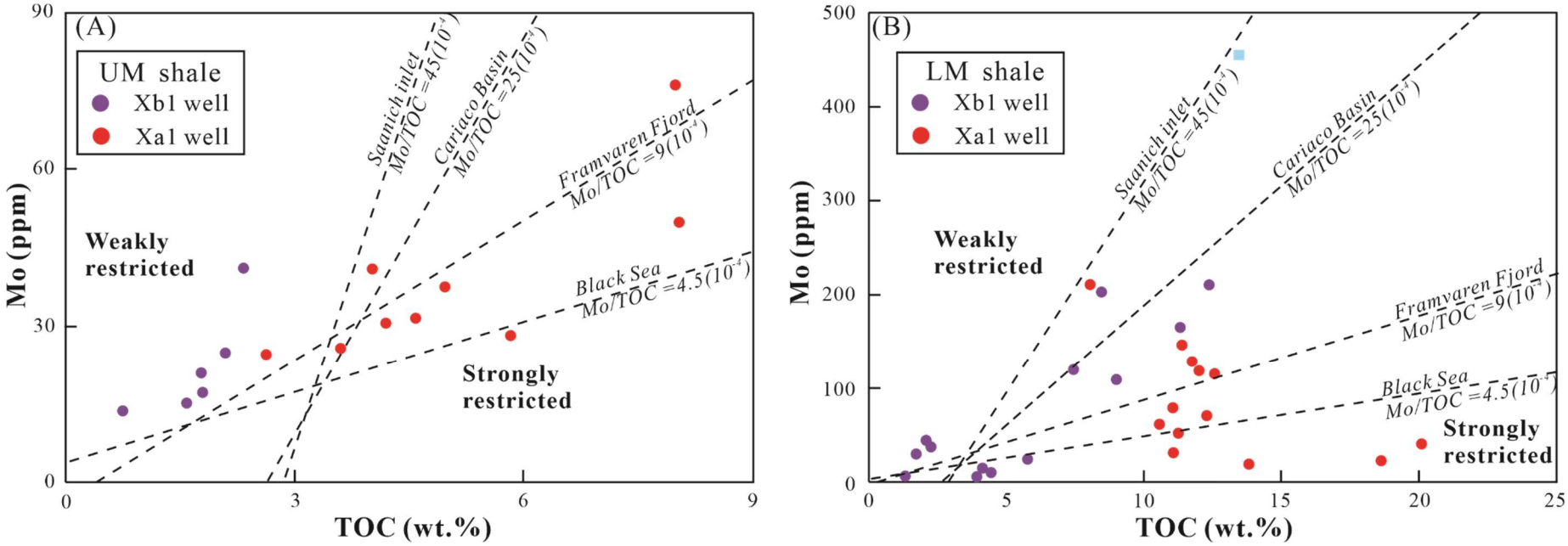
(A)
UM shale
Xb1 well
Xa1 well
Saanich inlet
Mo/TOC =45(10⁻⁴)
Cariaco Basin
Mo/TOC =25(10⁻⁴)
Framvaren Fiord
Mo/TOC =9(10⁻⁴)
Black Sea
Mo/TOC =4.5(10⁻⁴)
Weakly restricted
Strongly restricted
Mo (ppm)
TOC (wt.%)
0
30
60
90
0
3
6
9
(B)
LM shale
Xb1 well
Xa1 well
Saanich inlet
Mo/TOC =45(10⁻⁴)
Cariaco Basin
Mo/TOC =25(10⁻⁴)
Framvaren Fiord
Mo/TOC =9(10⁻⁴)
Black Sea
Mo/TOC =4.5(10⁻⁴)
Weakly restricted
Strongly restricted
Mo (ppm)
TOC (wt.%)
0
100
200
300
400
500
0
5
10
15
20
25

Figure 10

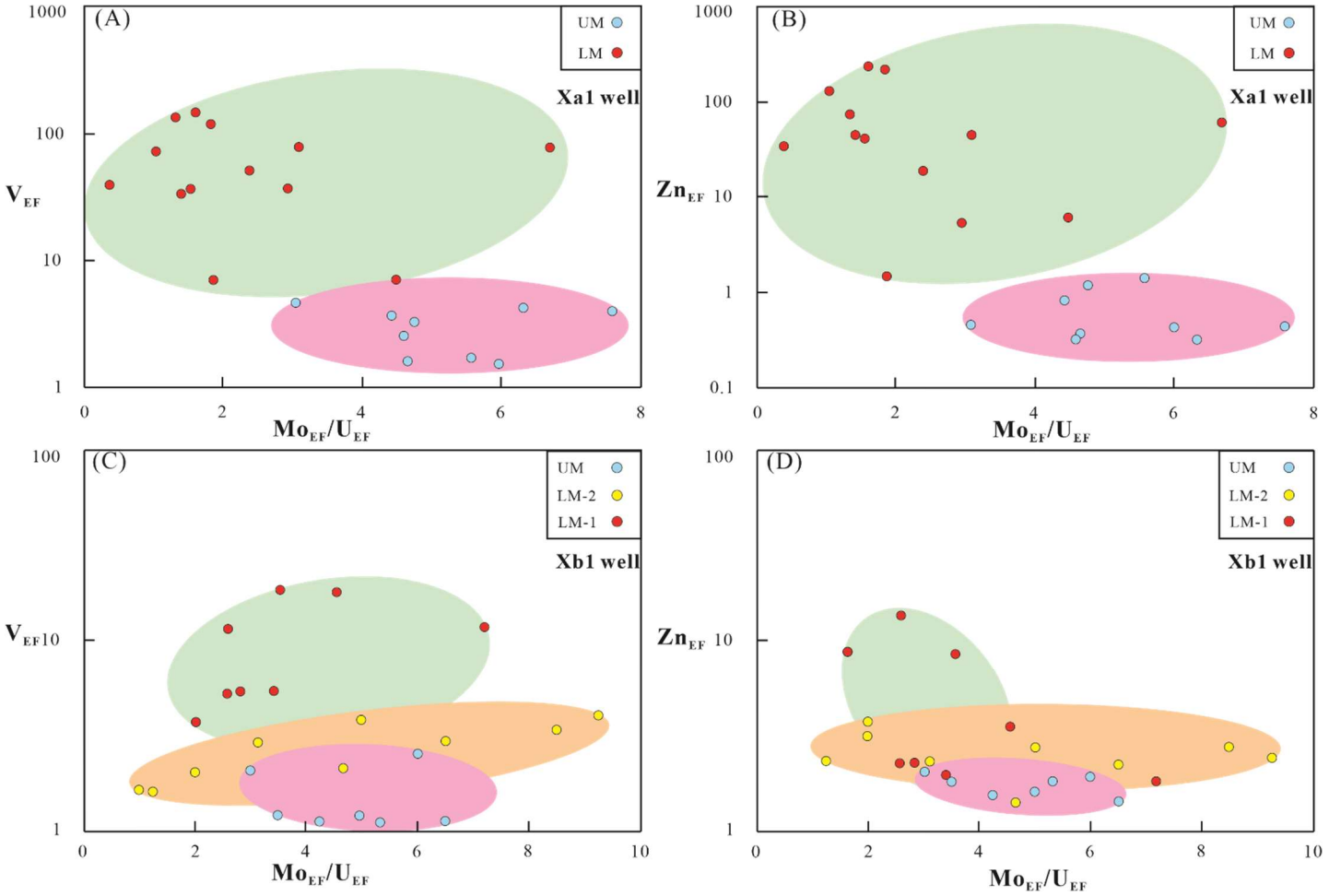
(A)
UM
LM
Xa1 well
1000
100
10
1
V_{EF}
0
2
4
6
8
Mo_{EF}/U_{EF}
(B)
UM
LM
Xa1 well
1000
100
10
1
0.1
Zn_{EF}
0
2
4
6
8
Mo_{EF}/U_{EF}
(C)
UM
LM-2
LM-1
Xb1 well
100
10
1
V_{EF}
0
2
4
6
8
10
Mo_{EF}/U_{EF}
(D)
UM
LM-2
LM-1
Xb1 well
100
10
1
Zn_{EF}
0
2
4
6
8
10
Mo_{EF}/U_{EF}

827 **Figure 11**

828

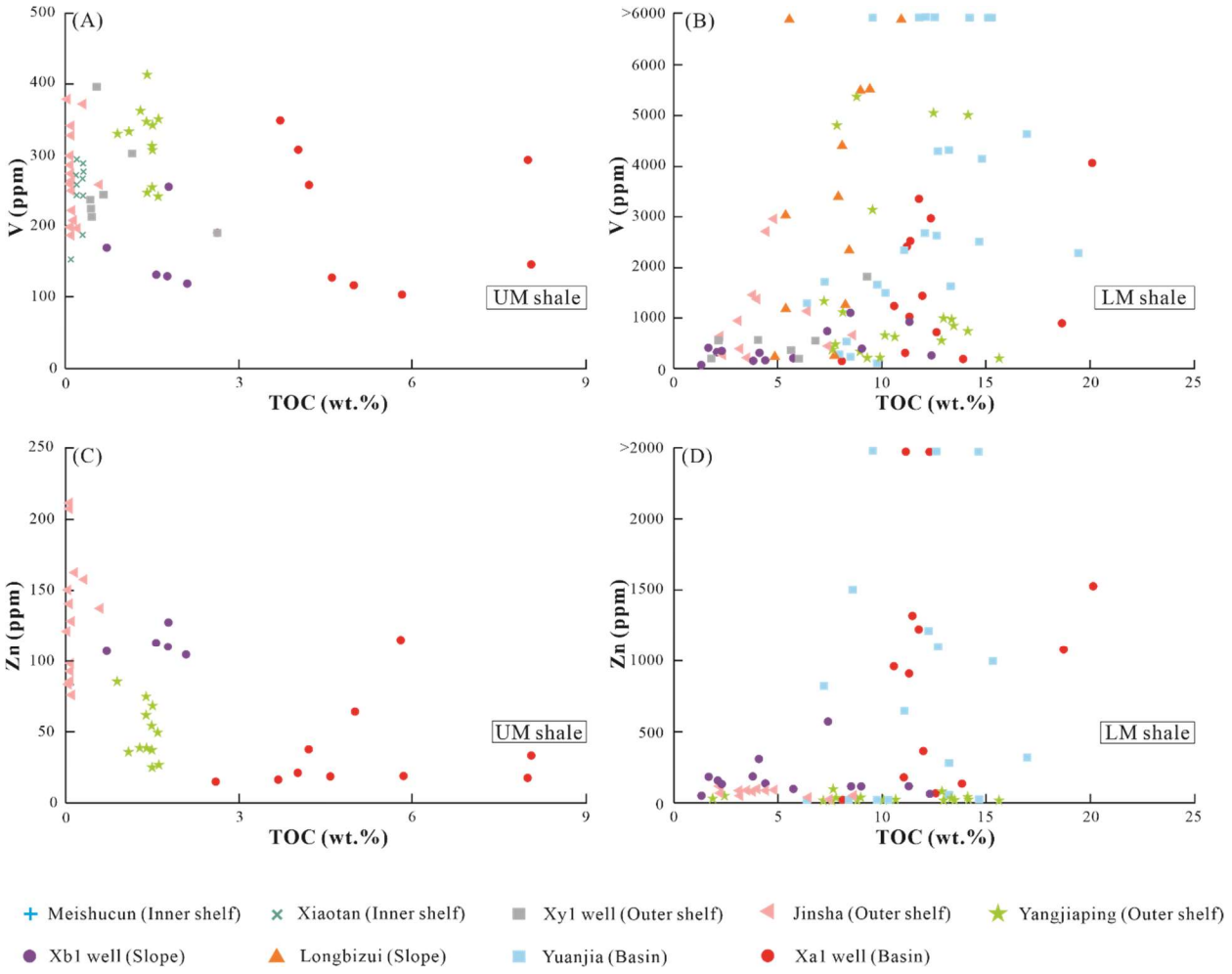

829

Figure 12

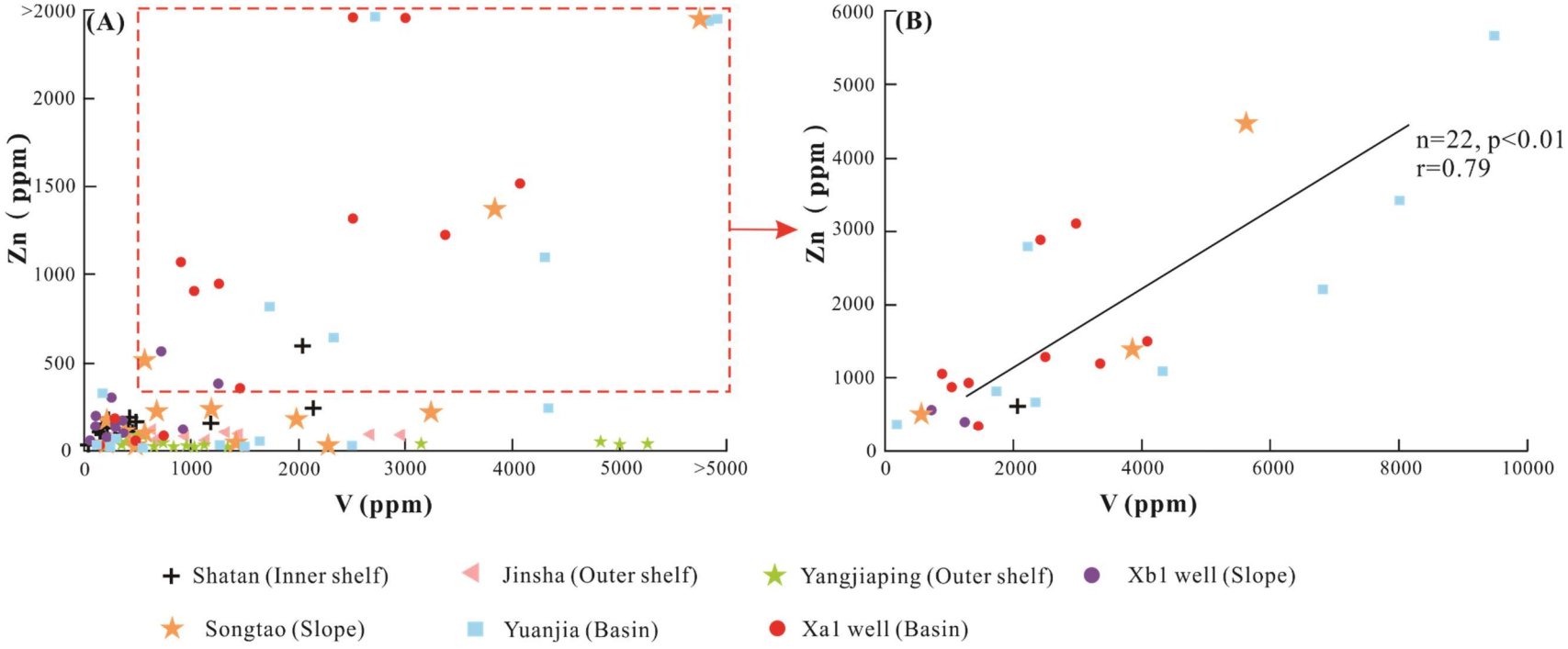
(A)
(B)
Zn (ppm)
V (ppm)
>2000
2000
1500
1000
500
0
>5000
5000
4000
3000
6000
8000
10000
n=22, p<0.01
r=0.79
Shatan (Inner shelf)
Jinsha (Outer shelf)
Yangjiaping (Outer shelf)
Xb1 well (Slope)
Songtao (Slope)
Yuanjia (Basin)
Xa1 well (Basin)

Figure 13

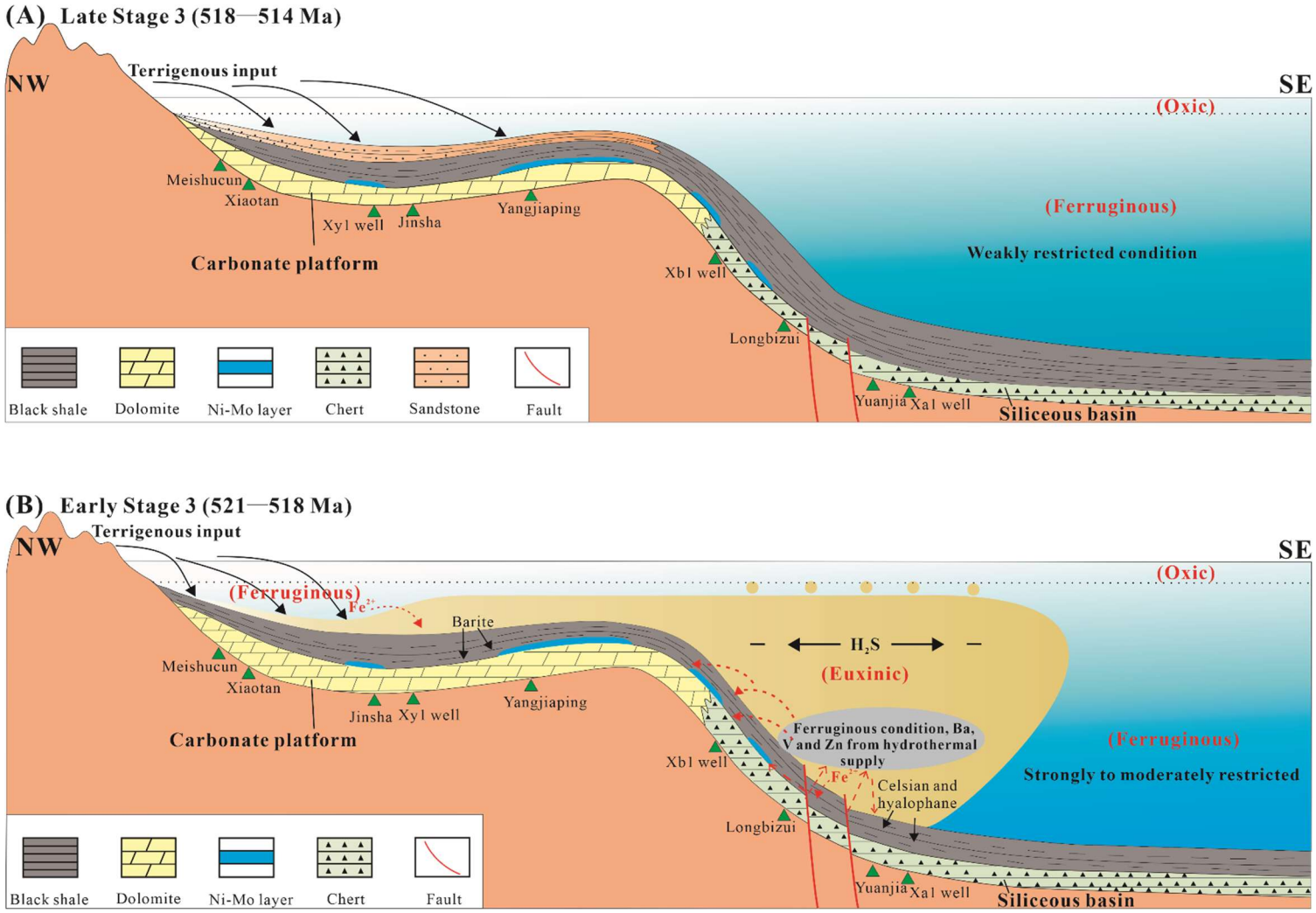
(A) Late Stage 3 (518—514 Ma)
NW
SE
Terrigenous input
(Oxic)
Meishucun
Xiaotan
Xy1 well
Jinsha
Yangjiaping
Carbonate platform
(Ferruginous)
Weakly restricted condition
Xb1 well
Longbizui
Yuanjia
Xa1 well
Siliceous basin
Black shale
Dolomite
Ni-Mo layer
Chert
Sandstone
Fault
(B) Early Stage 3 (521—518 Ma)
NW
SE
Terrigenous input
(Oxic)
(Ferruginous)
Fe2+
Barite
H2S
(Euxinic)
Meishucun
Xiaotan
Jinsha
Xy1 well
Yangjiaping
Carbonate platform
Ferruginous condition, Ba, V and Zn from hydrothermal supply
Fe2+
Celsian and hyalophane
(Ferruginous)
Strongly to moderately restricted
Xb1 well
Longbizui
Yuanjia
Xa1 well
Siliceous basin
Black shale
Dolomite
Ni-Mo layer
Chert
Fault